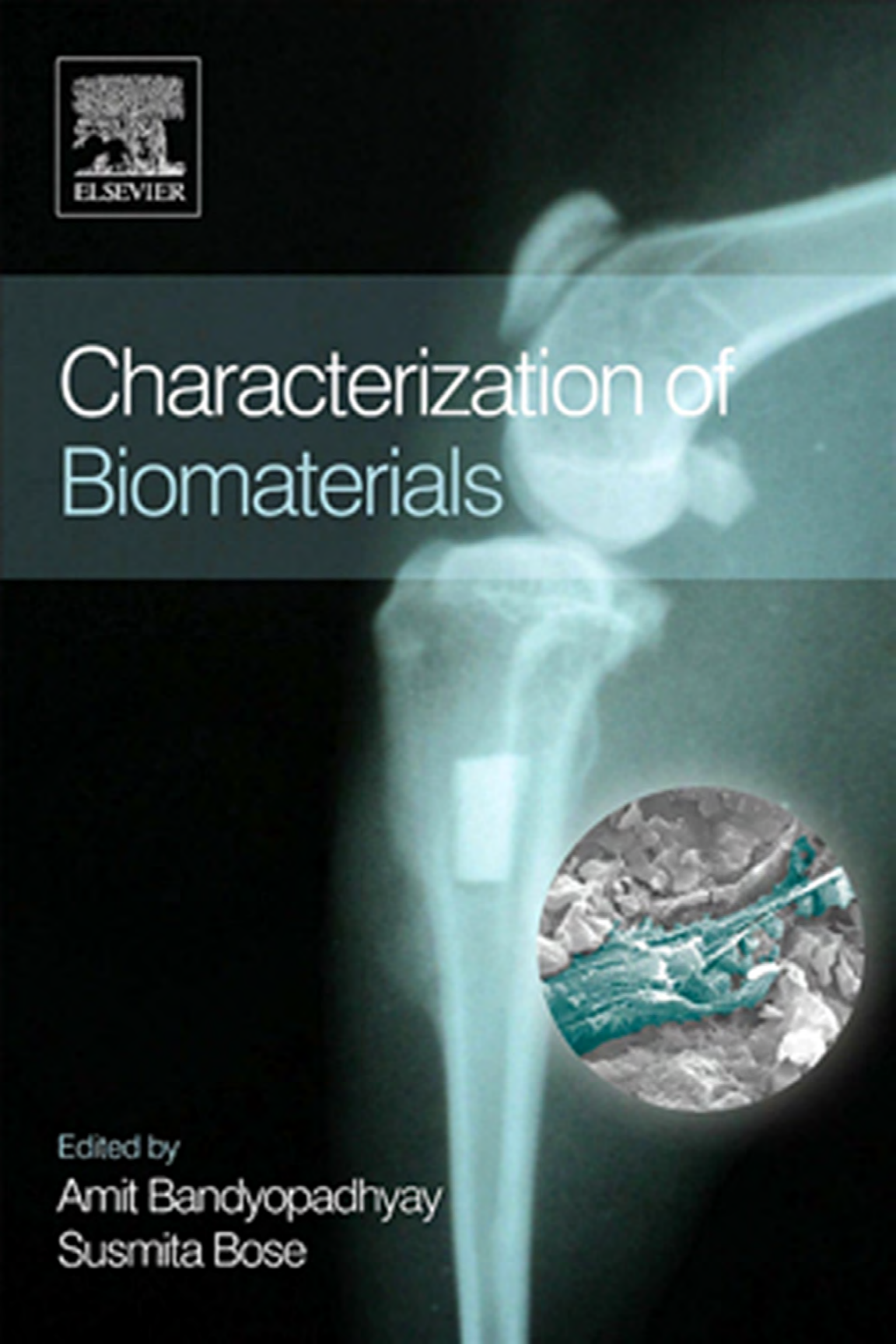
ELSEVIER
Characterization of Biomaterials
Edited by
Amit Bandyopadhyay
Susmita Bose

Characterization of Biomaterials

Edited by

Amit Bandyopadhyay
School of Mechanical and Materials Engineering
Washington State University
Pullman, WA, USA

Susmita Bose
School of Mechanical and Materials Engineering
Washington State University
Pullman, WA, USA

ELSEVIER

AMSTERDAM ● WALTHAM ● HEIDELBERG ● LONDON
NEW YORK ● OXFORD ● PARIS ● SAN DIEGO
SAN FRANCISCO ● SYDNEY ● TOKYO

Elsevier
225 Wyman Street, Waltham, MA 02451, USA
The Boulevard, Langford Lane, Kidlington, Oxford OX5 1GB, UK

Library of Congress Cataloging-in-Publication Data
Characterization of biomaterials / edited by Amit Bandyopadhyay, School of Mechanical and Materials Engineering, Fellow AAAS, ASM International, AIMBE and ACerS, Washington State University, Pullman, WA, USA, Susmita Bose, School of Mechanical and Materials Engineering, Fellow AIMBE, Washington State University, Pullman, WA, USA.
pages cm
Summary: "Characterization of Biomaterials will serve as a comprehensive resource for biomaterials researchers requiring detailed information on physical, chemical, mechanical, surface, *in vitro* or *in vivo* characterization. The book is designed for materials scientists, bioengineers, biologists, clinicians and biomedical device researchers seeking input towards planning on how to test their novel materials or structures or biomedical devices towards a specific application. Chapters are developed considering the need for both industrial researchers as well as academics"– Provided by publisher.
Includes bibliographical references and index.
ISBN 978-0-12-415800-9 (hardback)
1. Biomedical materials. I. Bandyopadhyay, Amit, editor of compilation. II. Bose, Susmita, editor of compilation.
R857.M3C47 2013
660.6'3–dc23
2012051185

British Library Cataloguing in Publication Data
A catalogue record for this book is available from the British Library

ISBN: 978-0-12-415800-9

Printed and bound in USA

13 14 15 16 17 10 9 8 7 6 5 4 3 2 1

Cover Credits:
1. Taxus Liberté drug-eluting stent - Courtesy Boston Scientific Corporation.
2. Bone cell-materials interaction on ceramic scaffold surface- Courtesy Mr. Gary Fielding, WSU, USA.
3. Radiographic image of 3D printed ceramic scaffold in rabbit femur - Courtesy Dr. Samit Nandi, WBUAFS, India.

Contents

Preface

The field of biomaterials is inherently multidisciplinary involving materials science, physical, engineering, biological and clinical sciences. Therefore, it is important for biomaterials researchers to understand what to and how to characterise different biomaterials. In recent years, there are quite a few good books published on introduction to biomaterials topic, however, no specific book is available towards how to characterise different biomaterials. The aim to develop this book was to focus primarily on biomaterials characterisation, something that can help graduate students and biomaterials professionals to learn specifically what techniques are good for testing certain biomaterial properties based on applications and how to do it. Moreover, what properties are good to test during materials development versus which properties should be tested during device development? These questions may be simple to some experienced biomaterials scientists, but many times hard to find answers for others. Considering these issues, this book is developed with specific emphasis towards characterisation of biomaterials and biomedical devices for their physical, mechanical, surface, *in vitro* and *in vivo* biological properties. Special attention was given towards device level characterisation for orthopaedic and cardiovascular implants. Chapters dealing with physical, mechanical and surface properties of biomaterials are developed by researchers from physical and engineering sciences. These chapters are focused on techniques that can reveal basic properties such as atomic structures, bonding, chemical interactions, phase identification and transformation, strength and toughness measurements, and property measurements at the surface level. Most of these techniques are followed by biomaterials researchers during early stage of materials development towards certain applications. The following chapters include *in vitro* and *in vivo* testing of biomaterials including microbial interactions and biofilm characterisation. These levels of testing are needed before a biomaterial can be considered for clinical trials or in actual device manufacturing. The final part of the book deals with device level characterisation with special emphasis on orthopaedic and cardiovascular devices. Researchers with industrial product development background contributed towards these chapters.

Apart from all the contributing authors, we also like to thank many of our students for their support towards developing this book particularly Mr Solaiman Tarafder, Mr Gary Fielding, Mr Himanshu Sahasrabudhe and Ms Sahar Vahabzadeh. We are also grateful to our boys, Shohom and Aditya,

without their cooperation we could not have completed this work. We hope that better understanding of biomaterials and biomedical device will not only save time but also will make them safer to use, a dream that resonates with every biomaterials researcher.

Susmita Bose and Amit Bandyopadhyay
Pullman, WA, USA
February 2013.

List of Contributors

Nehal I. Abu-Lail, Gene and Linda Voiland School of Chemical Engineering and Bioengineering, Washington State University, Pullman, WA, USA

Amit Bandyopadhyay, W. M. Keck Biomedical Materials Research Lab, School of Mechanical and Materials Engineering, Washington State University, Pullman, WA, USA

Haluk Beyenal, Gene and Linda Voiland School of Chemical Engineering and Bioengineering, Washington State University, Pullman, WA, USA

Subhasish Biswas, Department of Livestock Products Technology, West Bengal University of Animal & Fishery Sciences, Kolkata, India

Aldo R. Boccaccini, Institute of Biomaterials, University of Erlangen-Nuremberg, Erlangen, Germany

Susmita Bose, W. M. Keck Biomedical Materials Research Lab, School of Mechanical and Materials Engineering, Washington State University, Pullman, WA, USA

Hengchu Cao, Edwards Lifesciences LLC, One Edwards Way Irvine, CA, USA

Paul K. Chu, Department of Physics and Materials Science, City University of Hong Kong, Kowloon, Hong Kong, China

Rainer Detsch, Institute of Biomaterials, University of Erlangen-Nuremberg, Erlangen, Germany

Gautam Gupta, Biomet Inc, Warsaw, IN, USA

Imran Khan, Biomet Inc, Warsaw, IN, USA

T.S. Sampath Kumar, Department of Metallurgical and Materials Engineering, Indian Institute of Technology Madras, Chennai, India

Samit K. Nandi, Department of Veterinary Surgery and Radiology, West Bengal University of Animal & Fishery Sciences, Kolkata, India

Malcolm Naylor, Biomet Inc, Warsaw, IN, USA

Ryan K. Roeder, Department of Aerospace and Mechanical Engineering, Bioengineering Graduate Program, University of Notre Dame, Notre Dame, IN, USA

Mangal Roy, W. M. Keck Biomedical Materials Research Lab, School of Mechanical and Materials Engineering, Washington State University, Pullman, WA, USA

Chandra P. Sharma, Division of Biosurface Technology, Biomedical Technology Wing, Sree Chitra Tirunal Institute for Medical Sciences and Technology, Trivandrum, Kerala, India

Y.M. Thasneem, Division of Biosurface Technology, Biomedical Technology Wing, Sree Chitra Tirunal Institute for Medical Sciences and Technology, Trivandrum, Kerala, India

Huaiyu Wang, Department of Physics and Materials Science, City University of Hong Kong, Kowloon, Hong Kong, China

Julia Will, Institute of Biomaterials, University of Erlangen-Nuremberg, Erlangen, Germany

Ming H. Wu, Edwards Lifesciences LLC, One Edwards Way Irvine, CA, USA

Chapter 4

Surface Characterization of Biomaterials

Huaiyu Wang and Paul K. Chu
Department of Physics and Materials Science, City University of Hong Kong, Kowloon, Hong Kong, China

Chapter Outline

Characterization of Biomaterials. http://dx.doi.org/10.1016/B978-0-12-415800-9.00004-8

4.1. X-RAY PHOTOELECTRON SPECTROSCOPY

X-ray photoelectron spectroscopy (XPS), which is also called electron spectroscopy for chemical analysis, is the most widely used analytical technique to monitor the surface chemistry of solid materials due to its simplicity, flexibility, and sound theoretical basis. The typical XPS instrument includes an ultra-high vacuum system, X-ray source, electron energy analyzer, and data acquisition system. In XPS, the sample surface is irradiated by monochromatic X-ray and the emitted photoelectrons are detected. Figure 4.1 describes the general mechanism of photoelectron creation [1,2] and the energy of the photoelectron is given by:

$$E_B = h\nu - \mathrm{KE},$$

where E_B is the binding energy of the electron in the atom, $h\nu$ is the energy of the X-ray source (a known value in the experiment), and KE is the kinetic energy of the emitted electron that is measured. E_B is usually expressed in electron volts (eV) and 1 eV $= 1.6 \times 10^{-19}$ J. Since there are different electrons and binding energies in an atom, each element produces a set of unique peaks in the photoelectron spectrum and the peak intensity is a direct measure of the elemental concentration. As XPS is extremely surface sensitive, surface contamination can lead to stray results. XPS can provide qualitative and quantitative information on all elements except hydrogen and helium and furthermore, the shape of each peak and the exact binding energy can be slightly altered by the chemical state of the emitting atom. Hence, XPS can provide chemical bonding information as well.

XPS is typically performed by first taking a survey scan covering a range of 1000 eV and then, smaller energy ranges indicative of specific features are subsequently scanned in higher resolution. Survey scans are often in low resolution and are used to identify as well as quantify in terms of atomic percentage of major elements present on the materials surface. The *x*-axis is generally the 'binding energy' and the *y*-axis is typically 'intensity' or 'number of counts'. Readers are referred to excellent papers in the literature on how to identify and quantify elements from survey XPS data [3–10]. As an example, the typical survey spectra acquired from biomedical polytetrafluoroethylene films before and after plasma surface modification are illustrated in Fig. 4.2a

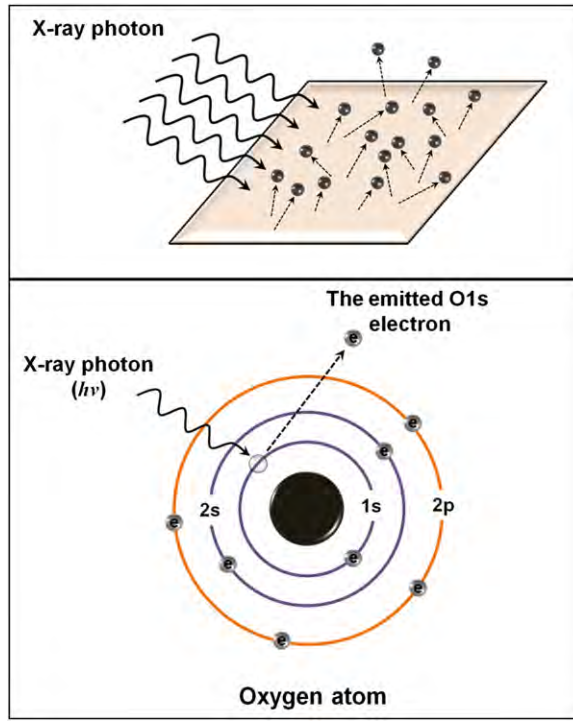

FIGURE 4.1 (Top) A surface irradiated by X-ray photons resulting in emission of photoelectrons and (bottom) the X-ray photon transfers its energy to a core-level electron imparting enough energy for the electron to leave the atom.

and b. As shown in the survey spectra, there are photoemission peaks associated with core-level photoionization events and X-ray-induced Auger electron peaks. Based on XPS handbooks [11,12], the photoelectron peak locations can be identified readily. The Auger lines are also usually listed in photoelectron peak tabulations and they can be readily distinguished from those of photoelectrons by changing the incident X-ray energy, for instance, using a Mg Kα source instead of an Al Kα source. The kinetic energies of Auger lines are invariable with incoming X-ray energy, whereas those of photoelectrons shift by the energy difference of the two X-ray sources. To obtain chemical bonding information, high-resolution scans are performed to cover a range of typically 20 eV or less and there are many associated publications in the literature [7–10,13]. Figure 4.2c and d displays the high-resolution C1s spectra acquired from the samples used to generate Fig. 4.2a and b, respectively. The spectrum in Fig. 4.2d is composed of a number of sub-peaks that convey chemical-state information about the carbon atom and details about the deconvolution can be

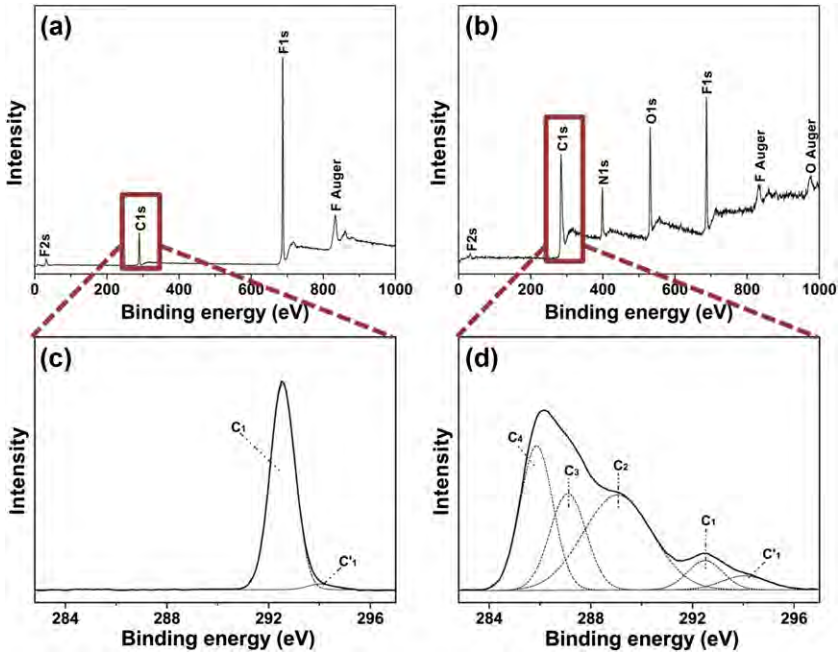

FIGURE 4.2 (a, b) XPS survey spectra and (c, d) high-resolution C1s spectra (c, d) acquired from biomedical polytetrafluoroethylene (PTFE) films before (a, c) and after (b, d) nitrogen/ammonia plasma immersion ion implantation: C_1 (F–C*–F), C'_1 (C_1 at the end of polymer chains), C_2 (–C*=O, –C*=NH, –C*–F), C_3 (–C*–NH_2, –C*–OH), and C_4 (–C*–H, –C*–C–).

found in the literature [14–18]. In addition to organic biomaterials, surface chemical information from inorganic biomaterials or inorganic coatings on organic biomaterials can be obtained [19–22]. However, the spectral features of other elements may be more complex. Heavier elements have other electronic orbitals such as p, d, and f and magnetic interaction between the electron spin (up or down) and orbital angular momentum may split the degenerate state into two components producing spin-orbit doublets. Figure 4.3 depicts the high-resolution Ti2p spectra acquired from TiO_2 before and after ultraviolet ozone treatments [22]. The Ti2p signals consist of both the $2p_{1/2}$ and $2p_{3/2}$ components with the separation resulting from spin-orbit coupling. In other cases involving transition elements, multiplet splitting can be observed.

Since only electrons emitted from the outermost surface of a few nanometres can escape without energy loss and be quantified, XPS is a much more surface sensitive technique than attenuated total reflection Fourier transform infrared (ATR-FTIR) spectroscopy, in which the IR beam can penetrate from several hundred nanometres to more than 1 μm. In order to collect elemental depth profiles, argon ion sputtering is performed in concert [23,24].

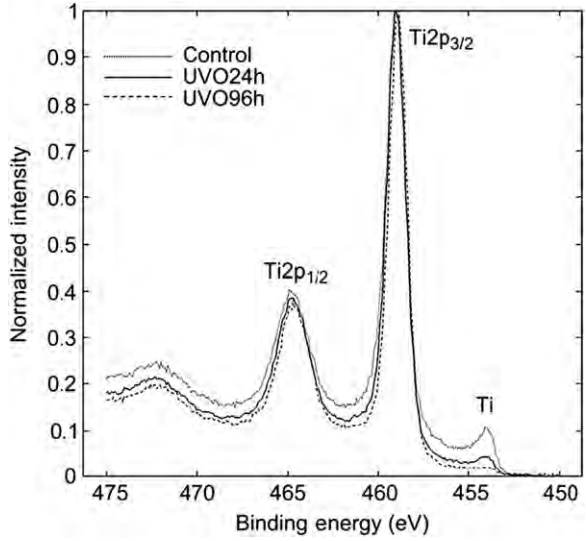

FIGURE 4.3 High-resolution Ti2p spectra obtained from TiO_2 before and after ultraviolet ozone (UVO) treatment. *Reprinted with permission from Ref. [22]. Copyright (2010) Elsevier.*

A representative depth profiling example is shown in Fig. 4.4 for a biomedical NiTi alloy after anodization and hydrothermal treatment. However, since argon ion sputtering can create damage, interpretation of chemical information requires care. Furthermore, ion beam mixing and associated effects such as atomic knock-on and sample roughening degrade the depth resolution, which is worse for a longer sputtering time (that is, deeper crater). Recently, it has been reported that accurate XPS depth profiles can be obtained from organic materials by using C_{60}^{+} [25–27] or coronene ($C_{24}H_{12}^{+}$) sputtering [28]. Figure 4.5 shows the XPS depth profile acquired from a drug-loaded PLA film using coronene as the sputtering ions [28,29].

In addition to depth profiling, recent improvements in the spatial resolution offered by commercial XPS systems enable more accurate and better XPS imaging capabilities [30–33]. Imaging XPS has been applied to biomaterials surface characterization and Fig. 4.6 illustrates an example [34]. As shown in the XPS images in Fig. 4.6, the P, N, and Na components are significantly increased after hybridization.

In conclusion, new instrumentation, technique development, and enhanced data analysis continue to expand the utility of XPS in biomaterials surface characterization. XPS provides survey spectra, high-resolution spectra, elemental depth profiles, and elemental maps using imaging. Although XPS is quite mature, new applications to biomaterials continue to be uncovered and the technique is expected to be a workhorse in biomaterials research, especially organic biomaterials such as polymers.

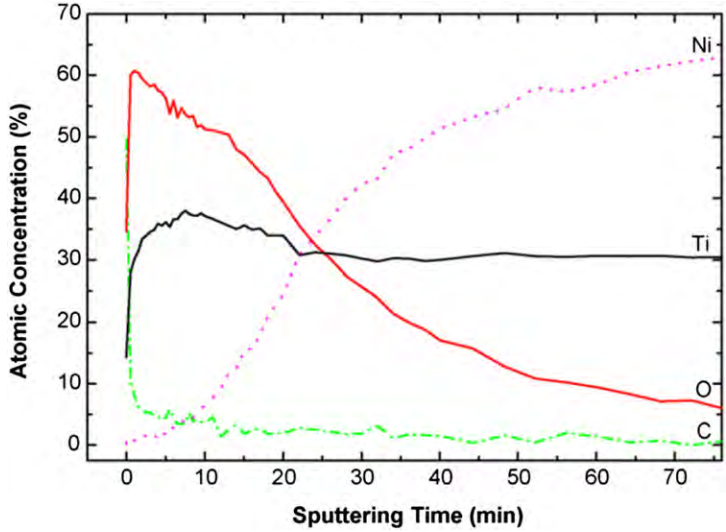

FIGURE 4.4 XPS elemental depth profiles obtained from nickel titanium alloy after anodization and subsequent hydrothermal treatment in water. *Reprinted with permission from Ref. [24]. Copyright (2007) Elsevier.*

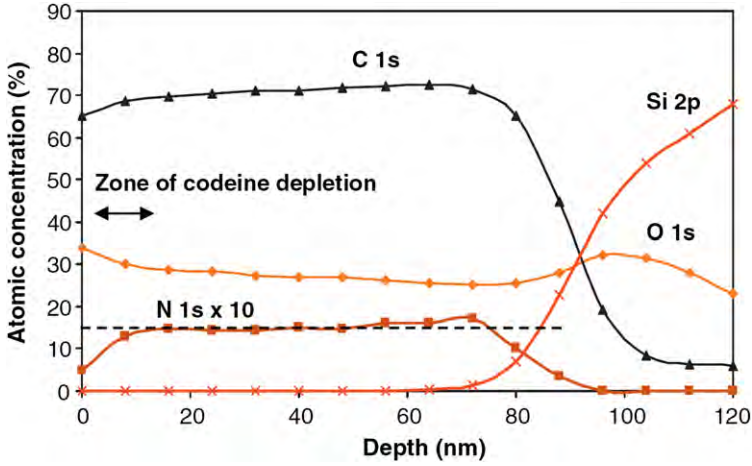

FIGURE 4.5 XPS depth profile acquired with a coronene ion source from a codeine-loaded PLA film showing atomic concentrations of C, O, Si, and N × 10. The N signal is unique to codeine and shows its depth distribution. The dashed line shows the theoretical N (×10) signal assuming uniform drug distribution through the film thickness. *Reprinted with permission from Refs [28,29]. Copyright (2009, 2011) Elsevier.*

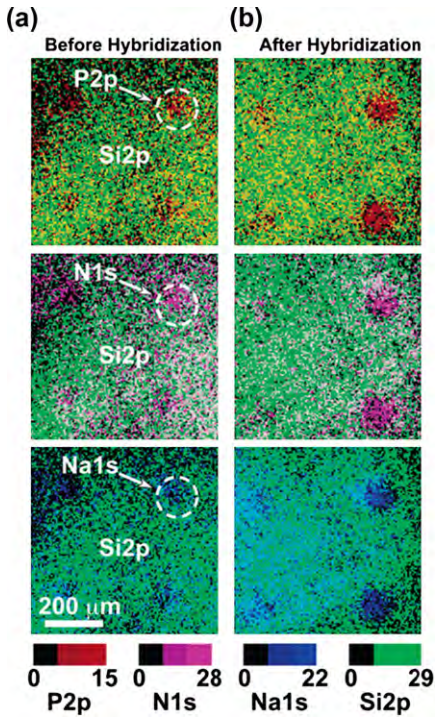

FIGURE 4.6 Superimposed XPS images of phosphorus (P2p), nitrogen (N1s), sodium (Na1s) with the substrate silicon (Si2p) signal intensity images (800 × 800 μm) from printed DNA probes on CodeLink microarray slides (a) before and (b) after target hybridization. *Reprinted with permission from Ref. [34]. Copyright (2007) American Chemical Society.*

4.2. AUGER ELECTRON SPECTROSCOPY

When electrons with energy between 3 and 30 keV bombard a solid surface, the Auger transition described in Fig. 4.7 takes place and Auger electrons carrying information about the host atom are emitted from the surface. The Auger process is related to three electrons at two different levels and the kinetic energy of an auger electron is determined by the energy difference of the singly ionized state and the double ionized final state. For an arbitrary ABC transition in an atom of atomic number z, the Auger electron kinetic energy is given by the difference in the binding energies of energy levels A, B and C [35] as

$$E_{\mathrm{ABC}}(z) = E_{\mathrm{A}}(z) - E^{*}_{\mathrm{B}}(z) - E^{*}_{\mathrm{C}}(z) - W_{\mathrm{s}},$$

where W_{s} is the spectrometer work function, A, B and C are the three energy levels of the Auger process involved (i.e. KLL, LMM, MNN – omitting the sub-levels), and E^{*} is the binding energy of a level in the presence of a core hole and is greater than the binding energy of the same level in a neutral atom. The kinetic energy of Auger electron depends on the atom and elemental information and can be obtained by Auger electron spectroscopy (AES).

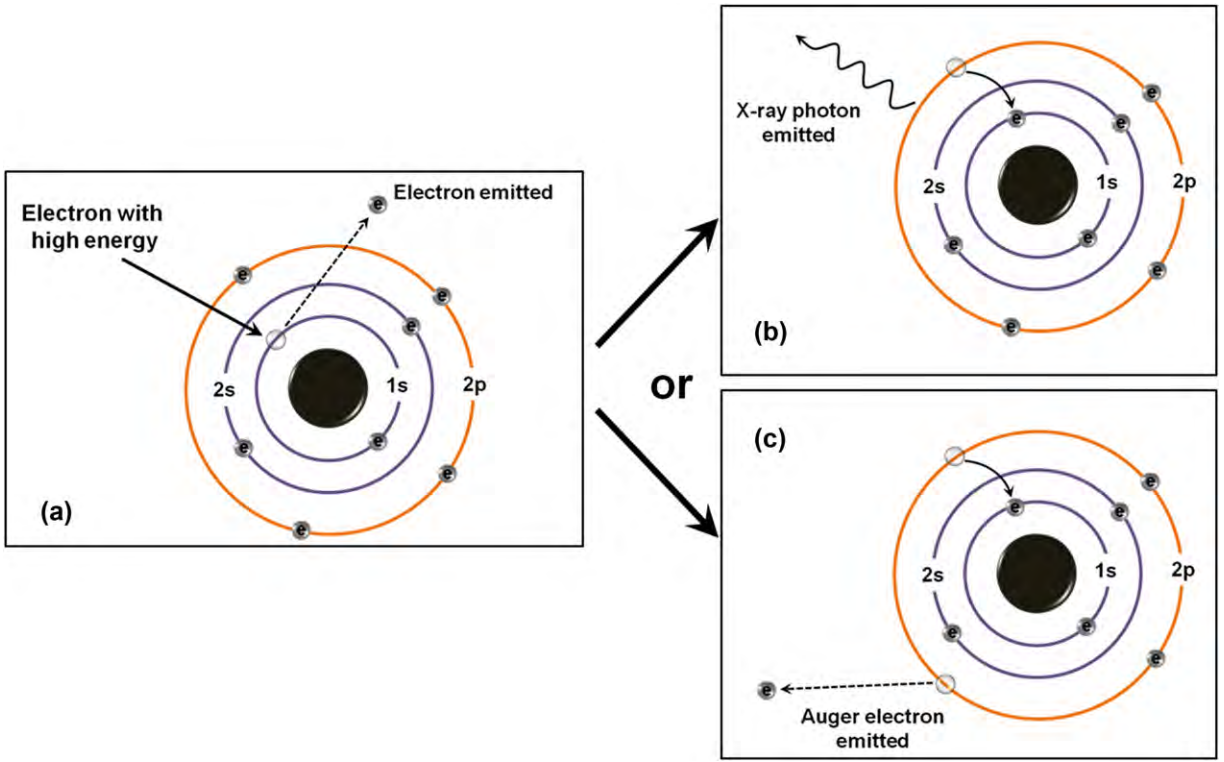

FIGURE 4.7 Schematic diagram illustrating the Auger electron emission process. (a) High-energy electron induces target atom with a core-level electron emission. (b, c) An electron drops from a higher energy level to the vacant core by (b) emitting X-ray or (c) ejecting an Auger electron.

AES is an important analysis tool for surface elemental and chemical identification. Similar to XPS, AES can detect all elements except hydrogen and helium in the outermost surface of a sample and depth profiles can be obtained when combined with ion beam sputtering. However, chemical shifts are less evident in AES compared to XPS although useful bonding information can be obtained in some cases. AES differs from XPS in several aspects. For instance, the electron spot size in AES is much smaller than the X-ray spot size in XPS and so, high-resolution imaging can be accomplished. Coupled with scanning, AES can be used to map the elemental distributions in the near-surface region and in-depth (with ion sputtering). However, because of charging, AES is not versatile as XPS in the analysis of insulating samples such as polymers and electron damage of organic samples can be severe and affects the results. Hence, contrary to XPS, AES is primarily used to study inorganic biomaterials [36–39]. For example, Hanzi et al. [36] treated the biomedical Mg–Y–RE alloy with thermal oxidation in air for different periods of time and as shown in Fig. 4.8, the elemental depth distributions are quite different. As aforementioned, owing to the excellent focusability of electron beams, AES can be used in elemental mapping of inorganic materials at very high spatial resolution [40–42].

4.3. SECONDARY ION MASS SPECTROMETRY (SIMS)

Secondary ion mass spectrometry (SIMS) is a sensitive technique to determine the elemental and molecular contents. Besides popular applications in semiconductors, new SIMS advances such as the time-of-flight technique enable the analysis of organic biomaterials. The surface sensitivity of low-bombardment-energy SIMS is quite high as the sampling depth is only about 1–2 nm compared to that of about 5–10 nm for XPS. Furthermore, it can detect all elements including hydrogen and helium as well as atomic ions and molecular ions at low concentrations. A basic SIMS instrument consists of three main components: the primary ion source, ion filtering system which selects ions with a defined energy, and mass spectrometer in vacuum.

No special sample preparation is required for SIMS, but similar to XPS and AES, the sample surface should be relatively free of adventitious contaminants from storage or transport. In SIMS, the sample surface is bombarded by ions or neutrals (normally between 1 and 40 keV). The momentum transfer initiates a collisional cascade, in which some atomic and molecular species are emitted as secondary ions. Ion mixing, knock-on, and sample roughening limit the depth resolution which depends on several instrumental factors such as primary ion energy, primary ion mass, and incident angle. Typical secondary ions originate approximately from the top two or three layers of the solid and have kinetic energy on the order from several to hundreds of electron volt. After leaving the solid surface, the positive or negative secondary ions are filtered by energy and mass-to-charge (m/z) ratio and detected by an electron multiplier or

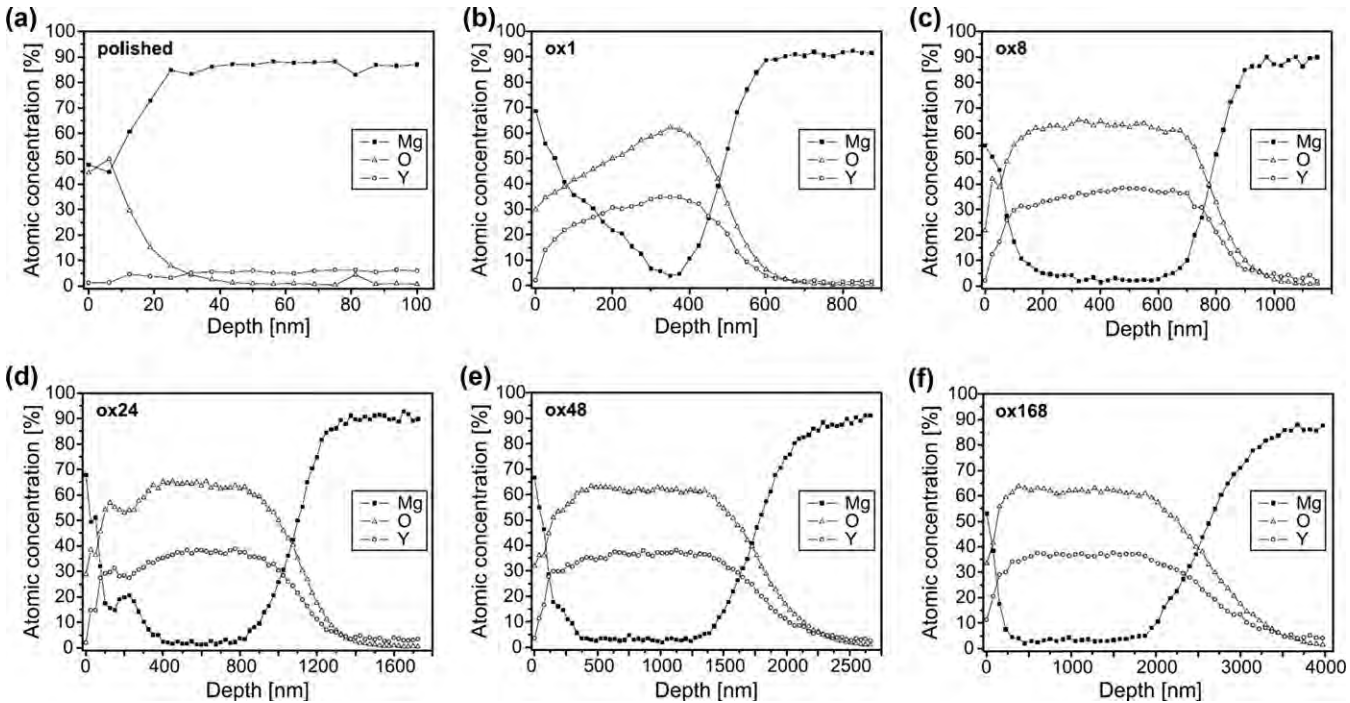

FIGURE 4.8 (a–f) AES depth profiles of Mg–Y–RE alloy: (a) Polished and after thermal oxidation in air at for (b) 1 h, (c) 8 h, (d) 24 h, (e) 48 h, and (f) 168 h. *Reprinted with permission from Ref. [36]. Copyright (2009) Elsevier.*

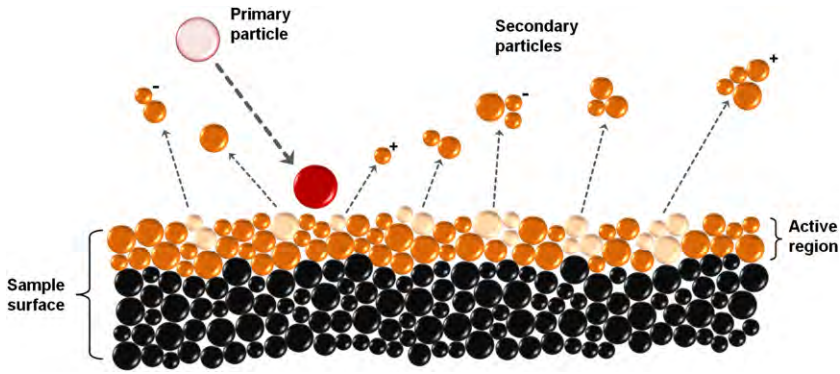

FIGURE 4.9 Schematic illustration of the secondary ion emission process initiated by the impact of a primary particle. Extensive fragmentation occurs near the collision site producing mainly atomic particles. Away from the point of impact collision, the process becomes less energetic resulting in the emission of larger molecular fragments.

image detector composed of micro-channel plates. The secondary ion fragments often impart characteristic information about molecular information and sometimes chemical information. A pictorial presentation of the sputtering process in SIMS is illustrated in Fig. 4.9 and more details can be found in the literature [43–49].

4.3.1. Static SIMS

There are two types of SIMS, dynamic and static. Dynamic SIMS, which is used in depth profiling analysis, is especially suitable for semiconductors. On the other hand, static SIMS uses a low-current primary ion beam (1 nA/cm^2 or less) in order to produce the least amount of surface damage in order to acquire molecular information to disclose the surface chemical structure. To avoid sample damage, there is a dose limit for static SIMS as 10^{13} ions cm^{-2}, but a value $\leq 10^{12}$ ions cm^{-2} is recommended. Static SIMS is a useful technique for biomaterials due to the excellent surface sensitivity and chemical (mass) selectivity. For instance, in protein adsorption experiments, static SIMS not only identifies the type of proteins present but also reveals the conformation, orientation, degree of denaturation, and other characteristics of the adsorbed protein not possible by XPS. Most proteins of interest have dimensions of 4–10 nm and the static SIMS spectrum of an adsorbed protein represents an amino acid assay of the outer 10–15 Å of the protein. Hence, if the distribution of amino acids in a protein is heterogeneous, the relative intensities of the amino acid fragments detected in the static SIMS spectrum are sensitive to the orientation of the protein on the surface and degree of conformational

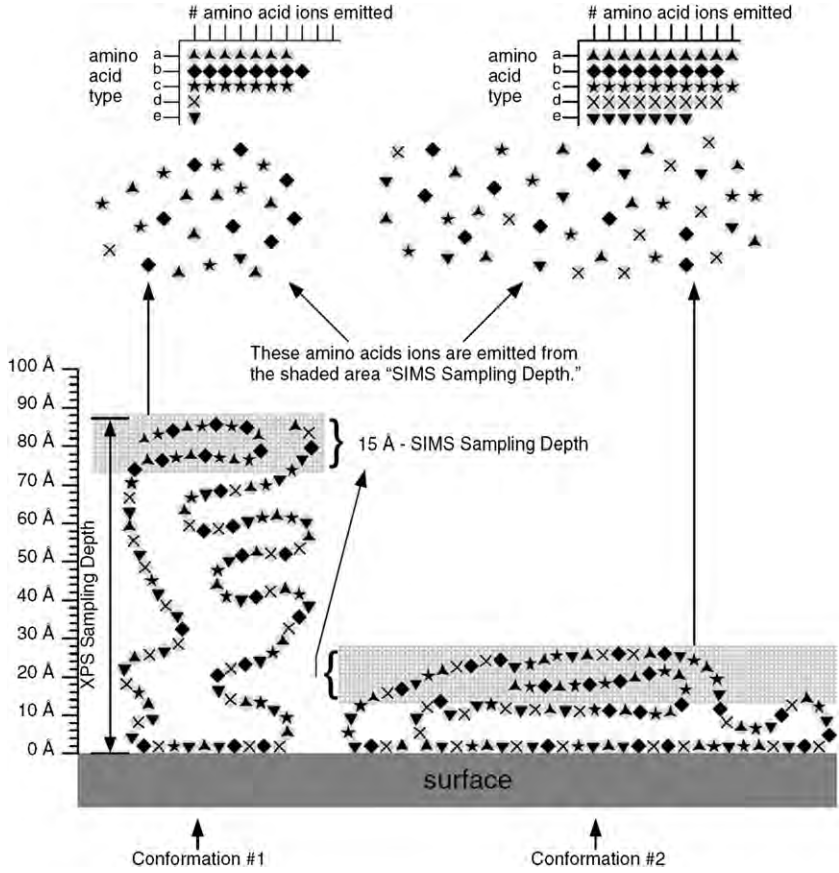

FIGURE 4.10 Schematic diagram of static SIMS investigation of the same protein with different conformation absorbed on the surface. A nonuniform distribution of those amino acids can produce different distributions of the detected amino acid fragments. *Reprinted with permission from Ref. [50]. Copyright (2001) John Wiley and Sons.*

alteration. When a protein adjusts to the surface and changes its conformation or orientation, new regions of the protein with different amino acid compositions are exposed for static SIMS. The schematic diagram of static SIMS study on the conformation of absorbed protein is depicted in Fig. 4.10 [50].

There are many published papers on the use of static SIMS on biomaterials characterization [51–54]. As shown in Fig. 4.11, Salerno et al. [53] compared the positive SIMS spectra acquired from a polymeric biomaterial (PEEK-WC-PU) before and after H_2/NH_3 plasma treatment. The new and more intense mass peaks at m/z of 18 (NH_4^+), 28 (CH_2N^+), and 30 (CH_4N^+) from the modified surface indicate that N-containing functional groups are successfully grafted onto the substrate. However, when studying a more complicated system such as

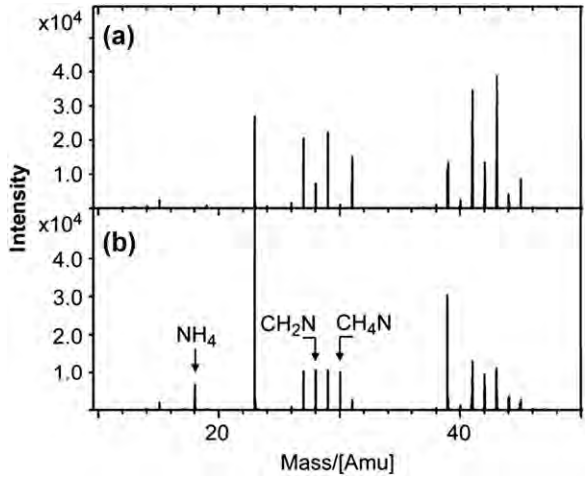

FIGURE 4.11 Positive-ion SIMS spectra of (a) pristine and (b) H_2/NH_3 plasma-modified PEEK-WC-PU membrane in the 10–50 m/z region. *Reprinted with permission from Ref. [53]. Copyright (2009) Elsevier.*

different conformation of the same adsorbed protein or different proteins absorbed on the same substrate, interpretation of all the secondary ions is complex and requires professional expertise. To overcome this difficulty, multivariate data analysis methods such as principal component analysis (PCA) are used to identify the major differences between SIMS spectra. With PCA, the dimensions of the SIMS spectra are reduced to a small number of variables called principal components, which are used to identify the differences among samples. A more rigorous description of the PCA can be found elsewhere [55] and applications of PCA analysis of static SIMS data to biomaterials research are increasing [56–58]. An example is illustrated in Fig. 4.12, in which the SIMS data are acquired from the ECM proteins (laminin, Matrigel, collagen I and collagen IV, respectively) on mica substrates [56]. Figure 4.12a shows that principal component 1 (PC1), which describes 60% of the total variance in the data set, successfully distinguishes collagen IV from the other three proteins. Principal component 2 (PC2) (describing 29% of total variances) separates the two collagens from laminin and Matrigel. Thus, by employing PC1 and PC2, these four kinds of proteins can be well differentiated. Figure 4.12b and c denotes the PCA loadings, which represent the relative abundance of one fragment versus another. As an illustration, a high positive loading for one fragment indicates that this fragment is present in a higher concentration in the sample with a high positive score. Likewise, fragments with high negative loadings indicate that the fragments are present in higher concentrations in samples with high negative scores.

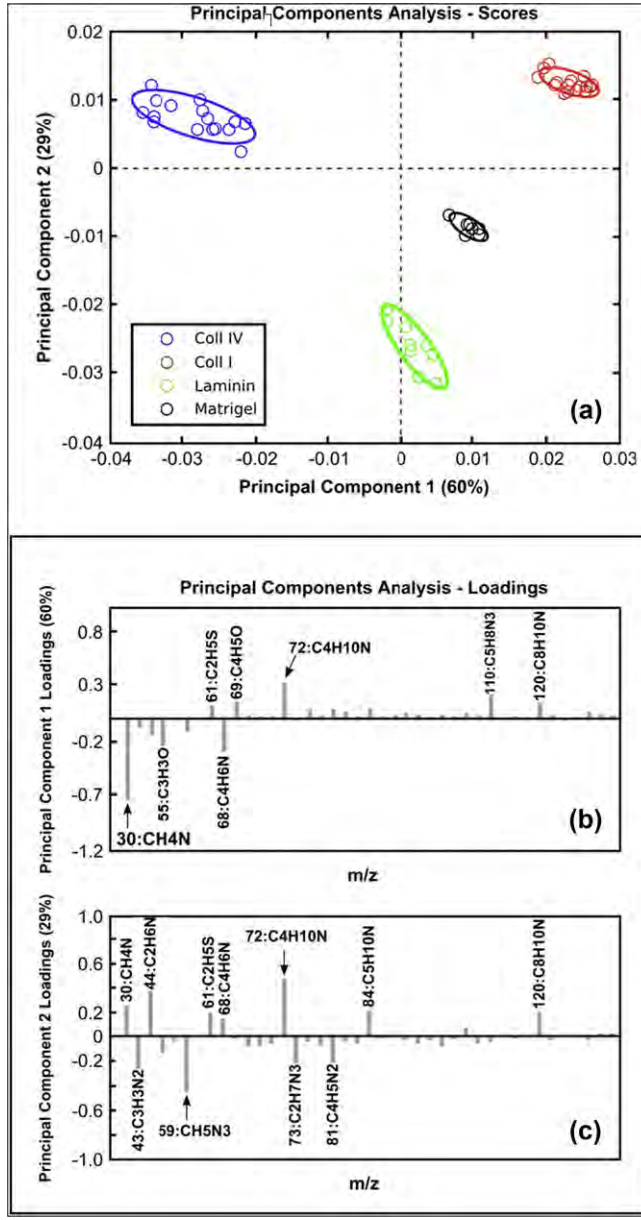

FIGURE 4.12 Principal component analysis (PCA) showing scores and loadings for SIMS data from protein films on mica. The protein samples are: collagen I (blue circles), collagen IV (red circles), laminin (green circles), and Matrigel (black circles). (a) is the PC1 versus PC2 scores plot, (b) shows the PC1 loadings, and (c) shows the PC2 loadings. *Reprinted with permission from Ref. [56]. Copyright (2011) Elsevier.*

On the heels of recent developments of SIMS instrumentations and applications of primary ions with higher secondary ion yields such as Bi^+, Bi_3^+, C_{60}^+, etc., static SIMS can provide chemical maps of biological or other complex materials in high spatial resolution [59–64]. The image resolution can be even higher in association with multivariate analysis methods (PCA and so on) to highlight the differences [65,66]. SIMS imaging is a powerful method to probe materials surface with complex chemistry, even chemical contrast can be verified in the sub-micrometre range [63,64]. For example, Ogaki et al. [64] fabricated chemically complex and patterned substrates (Au-Polymer-Au-SiO_2) by combining different processes including particle self-assembling, plasma eching (optional), plasma polymerization, sputtering, evaporating, and finally ultrasonication. The Au and SiO_2 regions on the substrates are selectively functionalized with fluorinated thiol and chlorinated silane, respectively, to yield local specific signals (F^- for Au and $^{35}Cl^-/^{37}Cl^-$ for SiO_2). As shown in the SIMS images in Fig. 4.13, the different regions are identified well by the unique fragments ions generated (HC^-, F^- and $^{35}Cl^-/^{37}Cl^-$) with high spatial resolution.

4.3.2. Dynamic SIMS

In dynamic SIMS, a high-current primary ion beam (1 μA cm^{-2} or greater) bombards the sample to erode the materials surface continuously while the real-time signals are recorded. The signal is plotted against sputtering time (or depth with proper calibration) to disclose the change in the elemental concentration with depth. Dynamic SIMS boasts several advantages such as high-depth resolution, high lateral resolution, excellent sensitivity, and high dynamic range. Unlike semiconductors, conventional dynamic SIMS is not popular in biomaterials characterization, especially for organic or protein absorbed biomaterials as sample damage from the primary ions is too severe resulting in information loss. There have been more applications to inorganic biomaterials [67] and dynamic SIMS can also be used to image cells labelled by different isotopes [68,69].

Polyatomic cluster ions as C_{60}^+ has been applied to SIMS characterization as the resulting damage cross-sections are much less than that of metal and metal cluster ions. This new technique expands the applications of dynamic SIMS to the characterization of organic materials not possible before. By using C_{60}^+ [70,71] or other ions [72] as the primary ions, the molecular depth profiles of the organic substrate can be obtained. As shown in Fig. 4.14 [70], the pure and different peptides deposited on silicon with trehalose films were characterized by dynamic SIMS with C_{60}^+ sputtering. It is clear that the signals of trehalose and the contained peptides remain constant until the entire film is removed and the Si substrate is reached, thus indicating the success of molecular depth profiling. With this new dynamic SIMS technique, 3D images of cells or organic substrates can be obtained without isotope labelling and more details can be found in the literature [73,74].

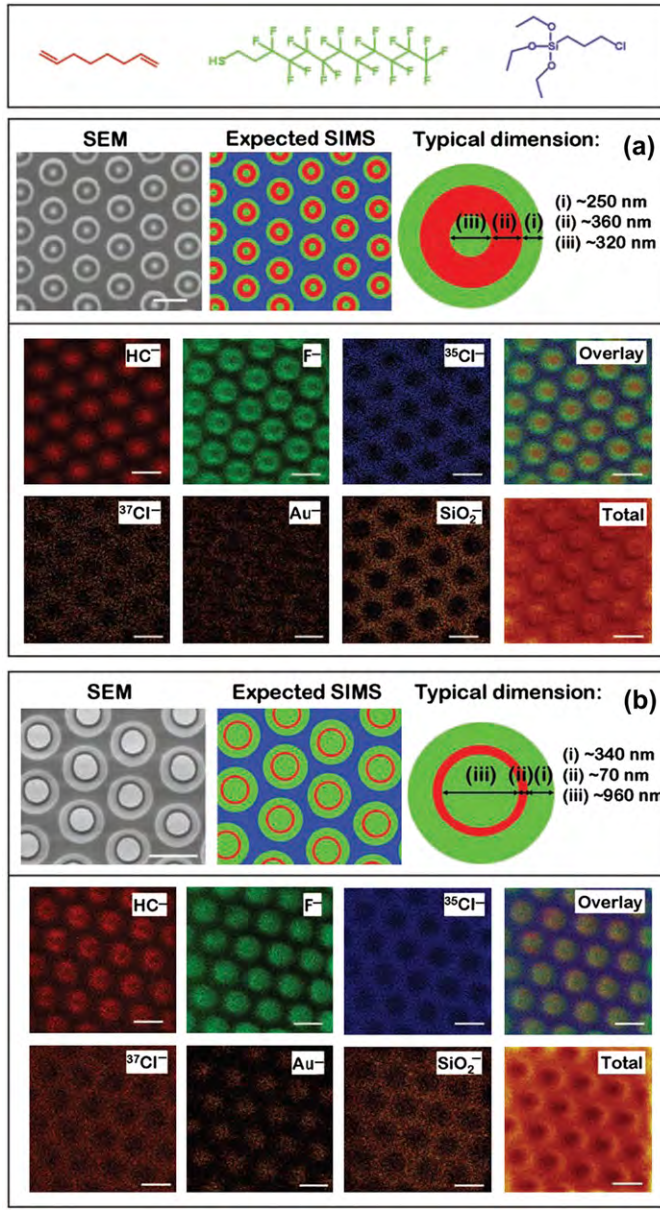

FIGURE 4.13 High-spatial-resolution negative-ion SIMS images of the Au-polymer-Au-SiO_2 surfaces with (a) 'small' Au and (b) 'large' Au central spots. The Au and SiO_2 regions are selectively functionalized with fluorinated thiol (top-center structure in green) and chlorinated silane (top-right structure in blue), respectively, and the monomer for polymer region is octadiene (top-left structure in red). The scale bar is 2 μm. *Reprinted with permission from Ref. [64]. Copyright (2011) John Wiley and Sons.*

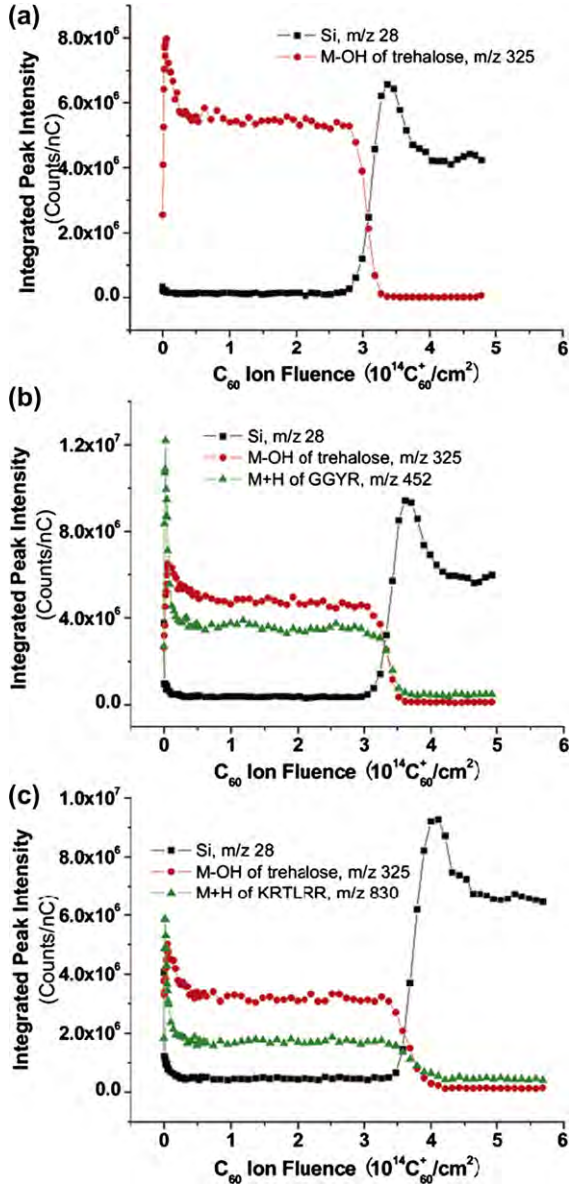

FIGURE 4.14 Secondary-ion signal intensities versus accumulated C_{60}^{+} ion fluence during depth profiling of (a) a pure trehalose film (270 nm), (b) a trehalose film doped with 1% GGYR (Gly–Gly–Tyr–Arg), and (c) a trehalose film doped with 1% KRTLRR (Lys–Arg–Thr–Leu–Arg–Arg). *Reprinted with permission from Ref. [70]. Copyright (2006) American chemical Society.*

In recapitulation, SIMS is a useful technique to obtain elemental and molecular weight information. By using static SIMS, the conformation, orientation, degree of denaturation, and other characteristics of adsorbed proteins can be studied. With the aid of multivariate data analysis, the major differences between complex SIMS spectra can be readily identified. Static SIMS is also effectively used to map biomaterials surface with complex chemical states with a spatial resolution better than that of XPS imaging. Molecular depth profiles and even 3D images can be obtained from organic biomaterials by dynamic SIMS using C_{60}^{+} as the sputtering ions. Although applications of SIMS to biomaterials are not as prevalent as those of XPS, the impact of SIMS is increasing with new technological development.

4.4. SURFACE MATRIX-ASSISTED LASER DESORPTION IONIZATION MASS SPECTROMETRY

Surface matrix-assisted laser desorption ionization mass spectrometry (Surface-MALDI-MS) is an extension of conventional MALDI-MS. In conventional MALDI-MS, a solution consisting of the analyte and a suitable matrix is laid on an MALDI plate, which is usually a specially designed metal plate. After the solvent evaporates, the analyte and matrix are co-crystallized. As the matrix usually has strong optical absorption in either the UV or the IR range, UV or IR lasers are employed and the matrix absorbs heavily the laser light, and then facilitates protonation (deprotonation) of the analyte molecules via a series of processes such as matrix ablation and ionization. MALDI-MS is a mass spectrometric method utilizing soft ionization and suitable for the analysis of biomolecules such as DNA and proteins as well as organic molecules like polymers and dendrimers, which tend to be fragile and easily fragmented if conventional ionization techniques are employed. A common problem for conventional MALDI-MS in that most biomaterials are solid and may not be easily dissolved by a solvent. On the other hand, surface-MALDI-MS can analyze adsorbed multicomponent bimolecular layers on the biomaterials by applying a direct coating with the matrix molecules to the sample surface. The matrix molecules that form on the surface are subsequently irradiated by a UV or an IR laser resulting in protonation (deprotonation) of the surface adsorbed entities. A pictorial representation of surface-MALDI-MS is illustrated in Fig. 4.15.

Surface-MALDI-MS is a relatively new surface analytical method for biomaterials. By desorbing the adsorbed macromolecules from the biomaterial surface and determining their molecular ions with high mass resolution and at levels below monolayer coverage, the detection limitation plaguing conventional MALDI-MS can be avoided. However, surface-MALDI-MS is not quantitative and requires control experiments and parallel XPS analyses for absolute quantification. In recent years, more work concerning surface-MALDI-MS has been performed. For example, Clarke et al. [75] employed surface-MALDI-MS to characterize albumin adsorption on different prepared

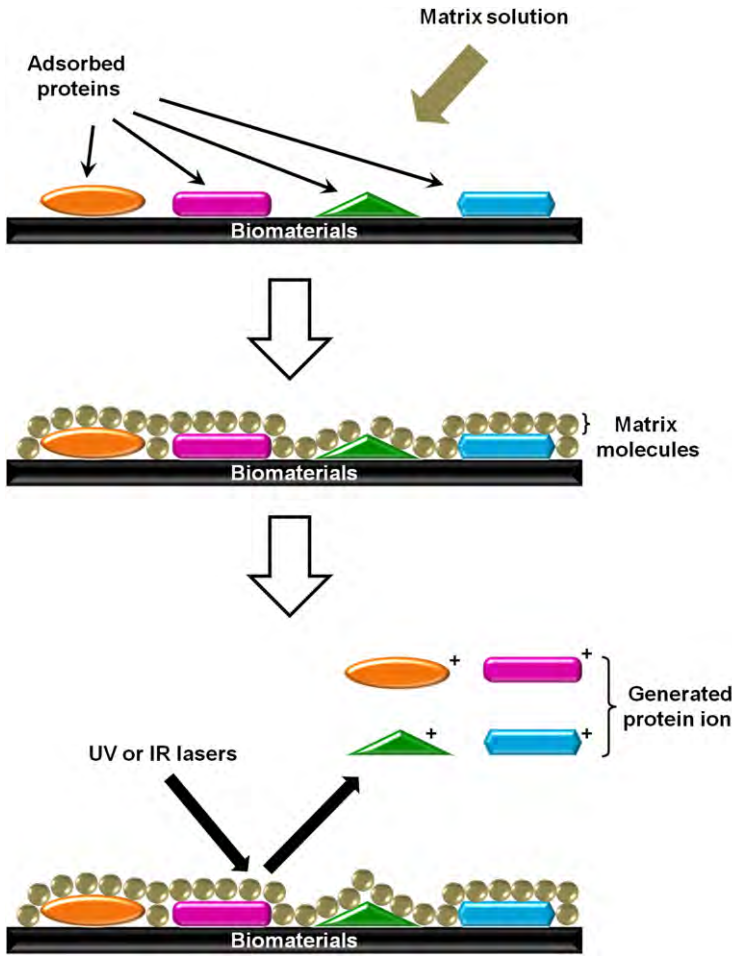

FIGURE 4.15 Schematic diagram of surface-MALDI-MS.

nitinol wires and observed that a nitinol wire with high nickel concentration and low oxygen concentration in the outer oxide layer was desirable for albumin adsorption. Heuts et al. [76] prepared various functionalized polyvinylidene fluoride (PVDF) substrates by ammonia plasma treating, star-poly(ethylene glycol) (PEG) coating, and star-PEG coating/Gly-Arg-Gly-Asp-Ser (GRGDS) peptide coupling and then assessed the surface protein repelling efficacy by surface-MALDI-MS. As shown in Fig. 4.16, insulin can only be detected on pure PVDF and ammonia-plasma-treated PVDF surfaces and albumin can only be detected on the pure PVDF surface. On the star PEG and biofunctionalized star PEG coatings, no insulin and albumin can be detected. There are other

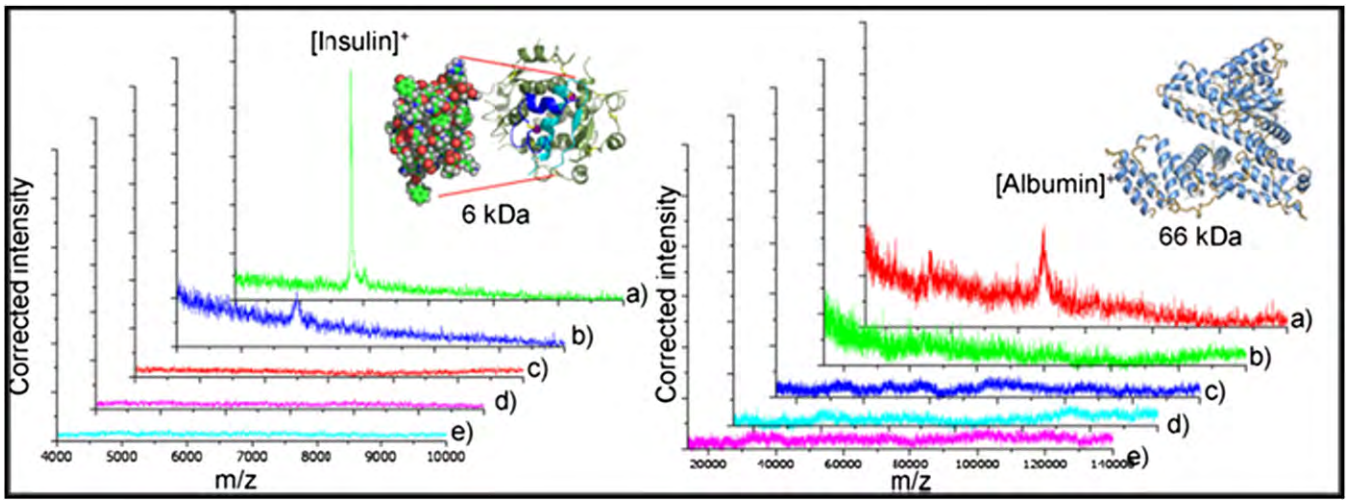

FIGURE 4.16 Surface-MALDI mass spectra of insulin (left hand side) and albumin (right hand side) on (a) pure PVDF, (b) ammonia plasma-treated PVDF, (c) star PEG-coated PVDF, (d) star PEG-coated PVDF biofunctionalized by consecutive coupling of 0.1 μmol mL^{-1} GRGDS, and (e) star PEG-coated PVDF biofunctionalized by consecutive coupling of 1.0 μmol mL^{-1} GRGDS. *Reprinted with permission from Ref. [76]. Copyright (2009) John Wiley and Sons.*

publications about Surface-MALDI-MS in biomaterials characterization [77–79] and interested readers are referred to a related review [80] for more information.

4.5. INFRARED (IR) SPECTROSCOPY

When a sample is irradiated by IR light, IR absorption occurs if the IR frequency coincides with the vibrational frequency of a bond. Hence, by monitoring the transmitted or absorbed IR light, information about the molecular structure can be obtained and this method is termed as IR spectroscopy. IR spectroscopy is the most widely used surface vibrational spectroscopy. As a surface chemistry studying tool, IR spectroscopy is attractive due to its versatility (applicable to almost any surface), compatibility with both high- and low-pressure conditions, and low cost compared to techniques requiring vacuum conditions. Most modern surface IR instrumentations, regardless of sampling mode, utilize a Fourier transform IR spectrometer rather than a grating monochromator in order to increase the signal level, enhance the photometric accuracy, and so on.

There are several modes of IR spectroscopy. The first one is transmission IR spectroscopy, which involves passing the IR beam through the sample. This mode requires at least partial transmission of the IR through the sample and so the acquired spectrum measures the bulk properties in lieu of the surface. Consequently, the transmission mode is rarely used in surface analysis of biomaterials, which also tend to be opaque to IR radiation. As an alternative, reflecting methods such as ATR IR spectroscopy and reflection absorption infrared spectroscopy (RAIRS) are more widely applied to surface characterization of biomaterials.

4.5.1. ATR IR Spectroscopy

ATR IR spectroscopy couples IR spectroscopy with total internal reflection to restrict the analysis volume. The IR spectrum is obtained from the substrate in contact with the internal reflection elements (IRE) such as zinc selenide or germanium. The IR radiation is first focused onto the end of the IRE at angles greater than the critical angle, enters the IRE, and is reflected down the length of the IRE. As shown in Fig. 4.17, at each internal reflection, the IR radiation actually penetrates a short distance from the surface of the IRE into the specimen. ATR IR spectroscopy is a powerful tool for the surface chemical characterization of opaque samples. However, it should be noted that as the penetration depth ranges from several hundred nanometres to more than 1 μm, ATR IR spectroscopy is not as surface specific as other analytical tools such as AES, XPS, and SIMS.

There are many applications of ATR IR spectroscopy to biomaterials [81–83] and generally, ATR IR spectroscopy is used qualitatively. For instance,

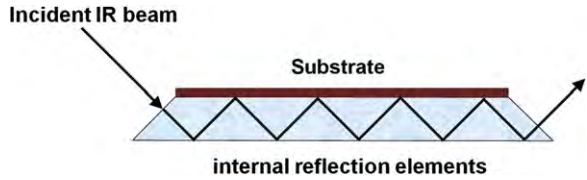

FIGURE 4.17 Schematic diagram showing the sampling IR beam passing through the internal reflection elements in contact with the opaque substrate.

Blaker et al. [82] produced biodegradable poly(D,L-lactide) with different proportional Bioglass® particles to form various composite samples with bioactivity and the ATR IR spectra reveal different chemistry. Rebollar et al. [83] altered the surface chemistry and topography of biomedical polystyrene foils by UV irradiation and as shown in Fig. 4.18, after irradiation, an intense and broad band centered at around 1720 cm^{-1} appears and can be attributed to the formation of carbonyl (C═O) containing species. Interpretation of the IR spectra is normally according to the IR handbooks [84,85].

4.5.2. Reflection Absorption Infrared Spectroscopy (RAIRS)

Greenler [86] demonstrated that for adsorbates on a metallic or conducting film, absorption of IR radiation by the adsorbate overlayer was enhanced at high angles of incidence (near grazing) and involved only one polarization of

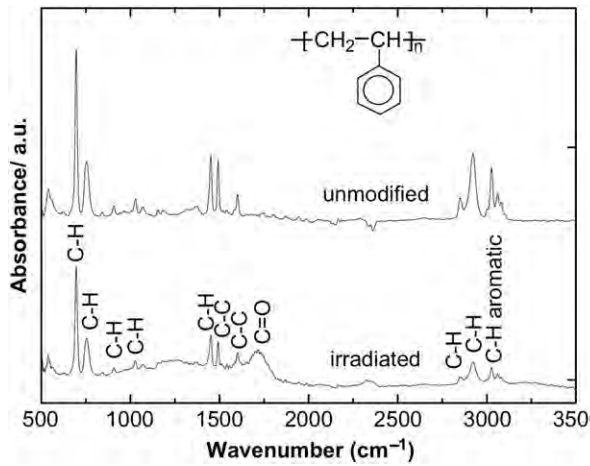

FIGURE 4.18 ATR IR spectra of unmodified polystyrene foil and UV irradiated polystyrene foil. The inset shows the chemical structure of polystyrene. *Reprinted with permission from Ref. [83]. Copyright (2008) Elsevier.*

the incident IR beam. RAIRS is based on this principle. RAIRS is very surface sensitive and particularly useful to the study of thin layers on a metal surface. Many types of biomaterials are surface-modified metals and so, RAIRS can be very useful [87–89]. Humblot et al. [88] functionalized gold surfaces with chemical groups and then covalently bound the anti-bacterial peptide (Magainin I). The RAIR spectra indicate successful binding of the functional agents. Briand et al. [89] fabricated a sample to serve as an immunosensor for goat anti-rabbit immunoglobulin (anti-rIgG) by immobilizing rIgG on a gold-coated substrate. After the sample was treated with solutions of labelled antigen with increasing concentrations, RAIRS was performed. As shown in Fig. 4.19, the characteristic amide I and amide II vibrational peaks (1660 and 1550 cm^{-1}) of the adsorbed antigen increase with antigen concentration, indicating that the sensitivity and specificity of this immunosensor are high. There are other IR methods available such as far-IR spectroscopy [90,91] and IR microscopy [92,93], but so far they are seldom used to characterize biomaterials.

4.6. RAMAN SPECTROSCOPY

When a light quantum $h\nu_0$ impacts a surface, an elastic scattering process termed *Rayleigh scattering* ensues. This process has the highest probability but there are also inelastic processes in which the vibrational energy is altered by $h\nu_s$. The inelastic process is called Raman scattering and an energy of $h\nu_0 \pm h\nu_s$

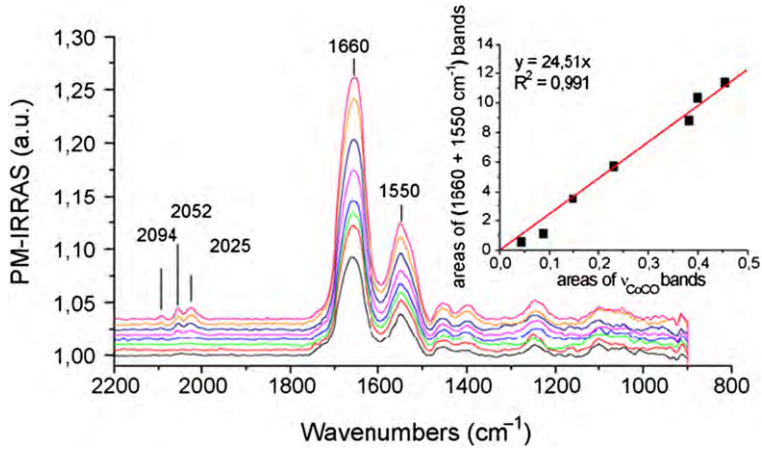

FIGURE 4.19 RAIRS response of the immunosensor to increasing concentrations of anti-rIgG labelled by cobalt-carbonyl probes in PBS containing goat serum (0.15%, v/v). Inset: Correlation between the areas of ν_{CoCO} bands and areas of amide I + II bands. The relative standard deviations are estimated to be equal to 0.1 a.u. for each IR area value. *Reprinted with permission from Ref. [89]. Copyright (2007) Elsevier.*

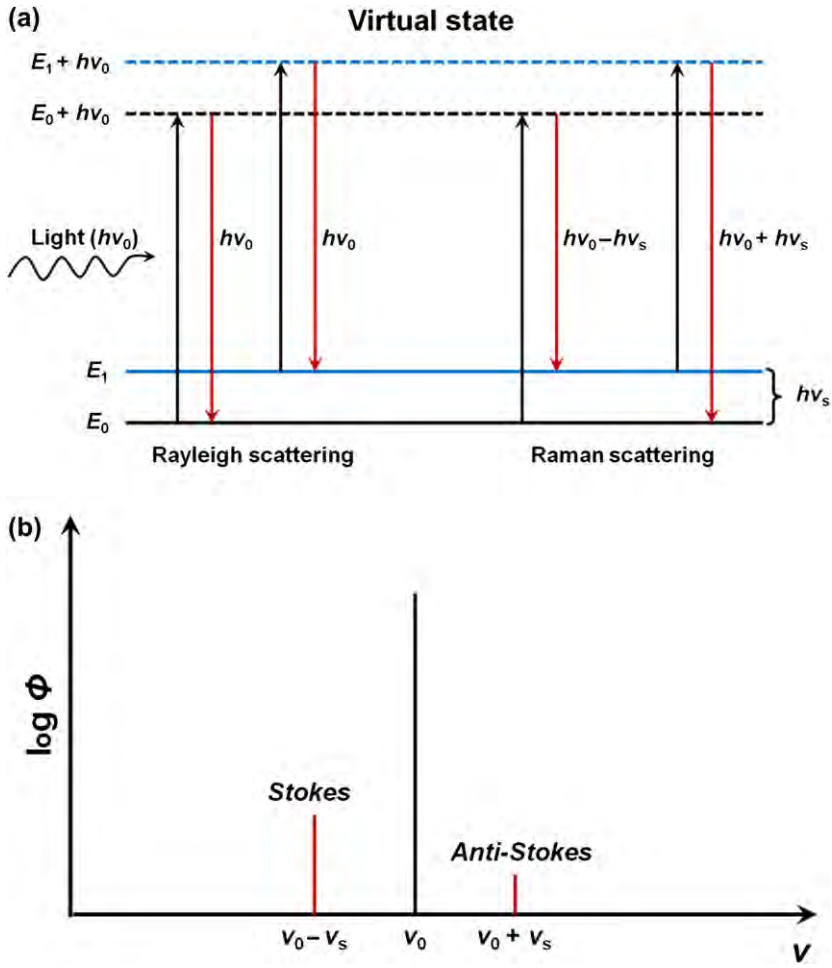

FIGURE 4.20 Schematic diagram showing the principle of Raman scattering: (a) term diagram and (b) related Raman spectra. Because the population of atoms in the excited state is much less than that of the ground state, the Stokes line is more intense than the anti-Stokes line.

is emitted. As shown in Fig. 4.20, when the incident radiation is absorbed by a virtual electronic state of the molecule, followed by emission back to the excited vibrational state, the emitted energy is $h\nu_0 - h\nu_s$ and the corresponding Raman lines are referred to as the *Stokes lines*. Alternatively, when the molecular vibration is already in the excited state and upon re-emission back to the ground state, the emitted energy is $h\nu_0 + h\nu_s$ and the Raman lines are called the anti-Stokes lines. As the population of molecules in the excited vibrational state is much less than that in the ground state at ambient temperature, the

emitted quanta having energy of $h\nu_0 - h\nu_s$ are more prevalent than those with energy of $h\nu_0 + h\nu_s$. As a result, the intensity of the Stokes lines is much higher than that of the anti-Stokes ones and normally, only the Stokes lines are monitored in Raman spectrum [94].

Raman spectroscopy is a powerful tool to investigate the surface chemistry of materials. Similar to IR spectroscopy, Raman spectroscopy is one of the molecular vibrational spectroscopies. IR and Raman are highly complementary as Raman spectroscopy is based on polarizability and IR spectroscopy is concerned with dipole moments. Sometimes, Raman spectroscopy is sensitive to those vibrational modes, which are either not observed by IR or give rise to only weak IR absorption bands. In Raman spectroscopy, the wavelength of the excitation source can be ultraviolet, visible, near-IR, and even IR. Its surface sensitivity is not only related to the excitation wavelength (exciting light with shorter wavelength penetrates a lower depth) but also concerned with the properties of the materials. Some modern Raman instruments are equipped with a microscope (particularly confocal microscope) to achieve higher spatial resolution and to eliminate fluorescence. Raman instruments can also be equipped with Fourier transform accessories to eliminate the fluorescence interferences but in this mode, the wavelength of the excitation source is fixed in the IR region and so, the advantages gained by working with visible or ultraviolet radiation are lost. Interpretation of Raman spectra is typically based on handbooks [85,94,95].

There are many examples of Raman spectroscopy applications to biomaterials and they are mainly divided into two parts. First and mainly, Raman

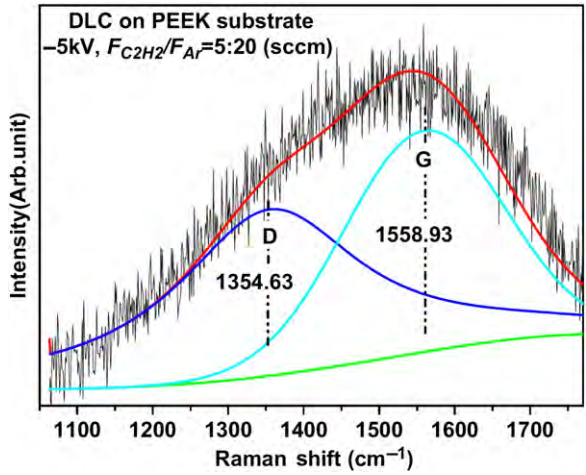

FIGURE 4.21 Gaussian–Lorentzion fitted Raman spectrum obtained from a biocompatible DLC film deposited on PEEK. *Reprinted with permission from Ref. [96]. Copyright (2010) Elsevier.*

spectroscopy is used to identify the chemical structure of biomaterials [96–99]. For instance, Wang et al. [96] deposited a diamond-like carbon (DLC) coating on poly aryl-ether-ether-ketone (PEEK) substrate to obtain better properties as a bone replacement. As shown in Fig. 4.21, the typical G band at 1558.93 cm^{-1} and D band at approximately 1354.63 cm^{-1} with the $I(D)/I(G)$ ratio of 1.2 are observed indicating successful DLC deposition on PEEK. Secondly, surface enhanced Raman scattering (SERS) by metals such as silver and gold has become a popular area and there are many publications about the use of metallic micro- or nano-structures in biosensors [100–102]. For example, Fang et al. [100] fabricated a series of Ag_2O mesocages with different shape such as mesosphere, mesododecahedron, mesocube and mesooctahedron. These Ag_2O mesocages were subsequently reduced to Ag with the same mesostructures and then deposited with crystal violet to serve as biosensors with SERS effects. As shown in Fig. 4.22, the Raman intensity

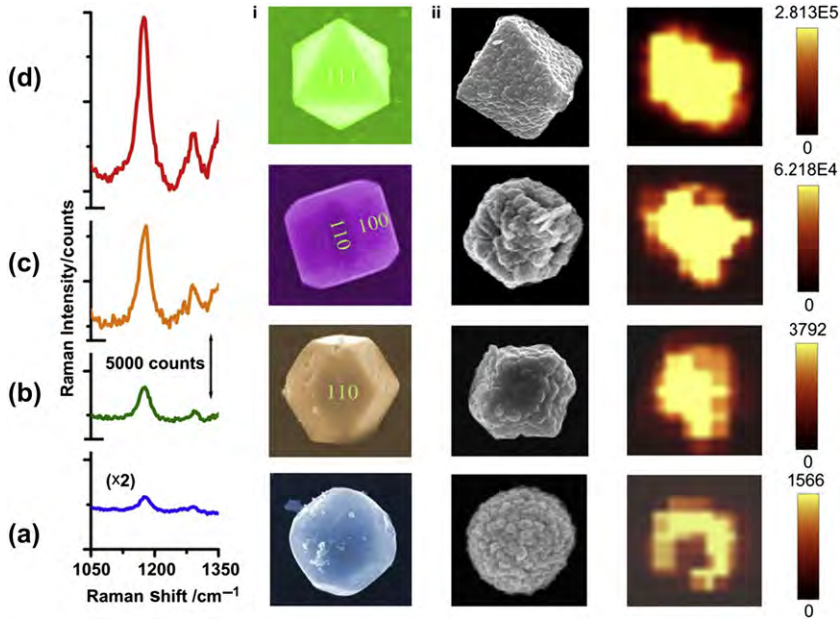

FIGURE 4.22 Single-particle SERS spectra and images of crystal violet (CV) on a polyhedral silver mesocages. a, mesosphere, b, mesododecahedron, c, mesocube, d, mesooctahedron. The color-coded signals of the right column correspond to the intensity of the Raman band of crystal violet (CV) at 1172 cm^{-1} integrated over 1120–1250 cm^{-1} after background subtraction. The spectra were acquired from individual silver mesostructures on Si substrates under the same conditions. CV was deposited onto the mesocages on Si substrates by drop coating a 10^{-9} M CV solution. Columns i and ii show the typical SEM images of individual polyhedral Ag_2O (i) and Ag (ii) mesostructures. *Reprinted with permission from Ref. [100]. Copyright (2011) Elsevier.*

of a single Ag mesooctahedron is much higher than that of the other three mesostructures, indicating the highest SERS effect. There are other techniques for biomaterials characterization based on Raman scattering such as Raman mapping which is generally used *in vitro* [102] or *in vivo* [103] and will be discussed in more detail in Chapters 5 and 6.

4.7. ELECTRON ENERGY LOSS SPECTROSCOPY

When a specimen is exposed to a beam of electrons with a narrow range of kinetic energy, some electrons undergo inelastic scattering accompanied by energy loss besides the more probable elastic scattering. As inelastic scattering is related to the sample properties, the amount of energy loss can impart useful information about the materials and this technique is termed electron energy loss spectroscopy (EELS). EELS as an analytical tool makes use of a series of inelastic interactions including phonon excitation, inter- and intra-band transitions, plasmon excitation, inner shell ionization, and so on. According to the geometry and kinetic energy of the incident electrons, EELS can be classified commonly into high-resolution EELS and transmission EELS.

In high-resolution EELS, electronic excitation of vibrational mode of the surface or molecules adsorbed on a surface is monitored by bombarding the sample with low-energy (1–10 eV) electrons and measuring the energy loss in the range of 10^{-3} eV to 1 eV. High-resolution EELS is a surface-sensitive vibrational spectroscopy, which plays an important role in the investigation of surface structure, catalysts, dispersion of surface phonons as well as monitoring of epitaxial growth. However, it is not often applied to biomaterials due to the rigorous experimental requirements and poor spectral resolution compared to IR spectroscopy and laser Raman scattering.

In comparison with high-resolution EELS, transmission EELS detects electrons with higher kinetic energy (typically 100–300 keV) and is typically coupled to a transmission electron microscope (TEM) to attain high spatial resolution. Because of the higher energy, the incident electrons can pass through specimens several hundreds of nanometres thick. Strictly speaking, transmission EELS is not a surface analytical technique, but nonetheless, transmission EELS is a unique tool for structural and chemical characterization of materials on the nanometre scale and can be combined with TEM, electron diffraction, and X-ray spectroscopy in the same instrument. According to the energy loss, the transmission EEL spectrum is usually divided into two regions, low-loss spectrum and core-loss spectrum. Low-loss spectroscopy is mainly used to investigate the changes in the plasmon peak. Not only the plasmon energy but also the plasmon peak widths are different for different materials. Core-loss spectroscopy is usually used to provide elemental information. The variations in the energy-loss near-edge structure of the element of interest can also be investigated. Transmission EELS is even capable of measuring the sample thickness based on $t/\lambda = \ln(I_t/I_0)$, where t is the absolute thickness, λ is

the mean free path, I_0 is the area under zero-loss peak, and I_t is the total area under the spectrum [104–106]. This equation can be implemented on each pixel yielding a semi-quantitative thickness map.

Despite high spatial resolution and useful information, transmission EELS is not commonly used in biomaterials characterization so far. This is probably due to the difficult sample preparation (the sample must be thin enough) and lack of hardware/operation expertise. Moreover, interpretation of EELS spectra may be complicated. Nevertheless, there are publications about characterization of biomaterials by transmission EELS [107–110]. For example, Ma et al. [107] prepared DLC coatings for blood interfacing application, then characterized the coatings by EELS with respect to sp^3 content investigation. Liou et al. [110] synthesized calcium-deficient hydroxyapatite nano-crystals with Ca/P ratios from 1.5 to 1.67 and EELS was subsequently used to characterize the structural disorder in samples.

4.8. ULTRAVIOLET–VISIBLE SPECTROSCOPY

Ultraviolet–visible (UV–vis) spectroscopy encompasses absorption spectroscopy and reflectance spectroscopy in the UV–vis spectral region. Molecules containing π-electrons or non-bonding electrons (n-electrons) can absorb ultraviolet or visible light energy and be excited to higher anti-bonding molecular orbitals. UV–vis spectroscopy is different from IR spectroscopy in the excitation wavelengths and that molecules undergo electronic transitions in the ultraviolet or visible region, whereas they undergo vibrational transitions in the IR region. Generally, UV–vis spectroscopy is used to determine elemental concentrations quantitatively in a solution according to Beer–Lambert law:

$$A = \mathrm{Log}_{10}(I_0/I) = \varepsilon cL,$$

where A is the measured absorbance, I_0 is the intensity of the incident light at a given wavelength, I is the transmitted intensity, L is the path length through the sample, c is the concentration of the absorbing species, and ε is a constant known as the molar absorptivity or extinction coefficient for each species and wavelength. Normally, ε at the wavelength of maximum absorption (λ_{max}) is employed in quantitative analysis as errors resulting from instrumental wavelength uncertainty are minimized at the peak of the absorbance curve. According to this relationship, the concentration of the analyte can be calculated when ε is known, L is fixed, and I_0 and I are measured. When a calibration curve of the analyte is available, the concentration of the analyte can be determined more accurately. Nevertheless, this application of UV–vis spectroscopy to biomaterials is not widespread because most biomaterials are not in a solution, the molar extinction coefficients of some biomaterials in a solution are unknown, and calibration curves are hard to get. Instead, a solution containing biomaterials is characterized by UV–vis spectroscopy to obtain the absorbance spectra rather than concentrations [111–113]. For example, Zhou

et al. [111] explored and evaluated the utilization of water-soluble nano-crystal CdTe quantum dots capped with negatively charged 3-mercapitalpropionic acid (MPA-CdTe QDs) to enhance the drug (daunorubicin) uptake into the targeted cancer cells. The UV–vis absorption spectra of the daunorubicin residue after cancer cells incubation reveal that MPA-CdTe QDs can effectively enhance the cellular uptake of this drug.

UV–vis spectroscopy is also available for the characterization of solid biomaterials on the nanometre scale when these nano-biomaterials are dispersed homogeneously in a solvent [114–117]. Lin et al. [115] fabricated magnetic nanoparticle (MNP) clusters by chemically linking Pluronic® F127 (PF127) to water-soluble polyacrylic acid-bound iron oxide (PAAIO) and further modified PF127-PAAIO with folic acid (FA) to obtain MNPs with tumor targeting properties. The content of FA decorated on MNPs is clearly indicated by the UV–vis spectrum of FA-PF127-PAAIO, in which a UV absorbance peak around 270 nm is attributed to the aromatic ring of FA. Mao et al. [117] employed UV–vis spectroscopy to measure the cloud points of the thermoresponsive copolymer [trimethyl chitosan chloride-g-poly(*N*-isopropylacrylamide)] which is used for gene transfection.

Besides the aforementioned examples concerning solvent-dispersed biomaterials, UV–vis spectroscopy can be utilized to measure the solid biomaterials in their natural states [118–120]. In this mode, only the surface regions of solid biomaterials are measured. For instance, van den Beucken et al. [118] fabricated two types of multilayered coatings, poly-D-lysine/DNA (PDL/DNA) and poly(allylamine hydrochloride)/DNA (PAH/DNA), on quartz substrates and then monitored the build-up of DNA coatings by UV–vis spectroscopy by measuring the absorbance maximum of the nucleic base chromophores in the DNA at 260 nm. Lee et al. [120] developed a multifunctional 4-bit biomemory chip that consisted of recombinant azurin variants

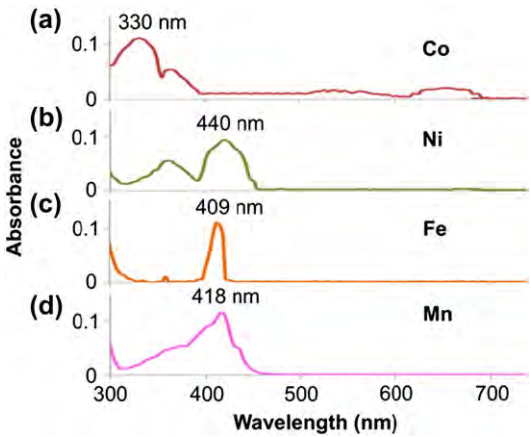

FIGURE 4.23 UV–vis absorption spectra of (a) Co-type azurin (b) Ni-type azurin (c) Fe-type azurin and (d) Mn-type azurin. *Reprinted with permission from Ref. [120]. Copyright (2011) Elsevier.*

when the Cu ion in this recombinant azurin protein was substituted with other metal ions such as Co, Mn, Fe, and Ni ion to allow the protein to perform various memory functions. UV–vis spectroscopy was subsequently performed to confirm the metal substitution, and the absorption spectra of different azurin proteins are shown in Fig. 4.23.

4.9. LIGHT MICROSCOPY AND CONFOCAL MICROSCOPY

Light microscopy, often referred to as the 'optical microscopy', utilizes visible light and a system of lenses to obtain magnified optical images. As one of the oldest analytical techniques, it is very popular in the scientific and industrial communities and applications include biomaterials characterization [121,122]. For instance, Ji et al. [121] fabricated 3,3′-dithiobis(propanoic dihydrazide)-modified HA (HA-DTPH) nanofibrous scaffolds by electrospinning and then employed light microscopy to map the surface after equilibrium swelling in air. The images in Fig. 4.24 reveal the morphological change on the sample surface after water evaporation for different time. However, because of basic physics, the spatial resolution of conventional light microscopy is limited and the intrinsic properties of focus (in-focus and out-of-focus information points contribute equally to the images) of this technique can lead to blurred images.

Confocal microscopy (CM), an improved light microscopy technique, can provide blur-free optical sectioning of a specimen by eliminating out-of-focus information through spatial filtering using a point source of light for excitation. Sample preparation is easier and high-resolution images can be more easily obtained by CM. The actual useful depth of CM is limited to approximately 100–200 μm and the image resolution is 0.18 μm in the *xy*-plane and about 0.35 μm in the *z*-plane. Three-dimensional structures can be reconstructed by carefully compiling two-dimensional images obtained.

CM is a powerful tool in various fields such as life science, semiconductors, and materials characterization. In the biomaterials field, it not only is a popular tool for the *in vitro* characterization (e.g. imaging cells seeded on the samples) [123–125] but also can be used on samples before cell culturing by mapping the surface and structure [122,126–129]. For example, Cross et al. [126] prepared hydrated collagen gels with different concentrations by mixing an acidic collagen solution with alkali solution, and then polymerized them into poly (dimethylsiloxane) (PDMS) moulds. CM was subsequently used to image the fiber structure of the collagen gels. Da Silva et al. [128] fabricated periodic hydrogel scaffolds with a 3D honeycomb-like structure from colloidal crystal templates and then examined the surface and structure by CM. As shown in Fig. 4.25, a series of confocal slices (a) can be obtained at different depths (the surface, middle of the first layer, and even deeper) of the fabricated hydrogel scaffolds. CM can also map the z-projection (b) and construct the three-dimensional structure (c) of a segment from the same stack. The use of

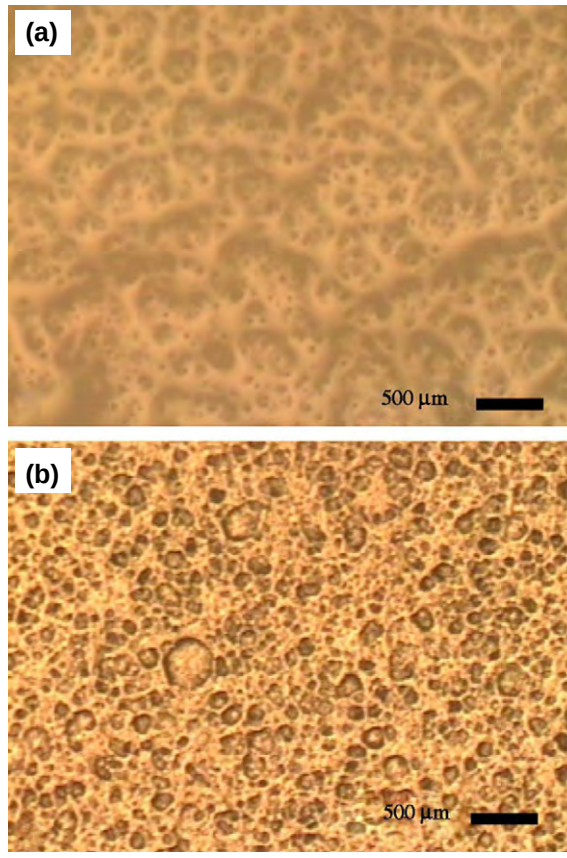

FIGURE 4.24 Optical images of HA-DTPH nanofibrous scaffold after equilibrium swelling in air for (a) 30 min and (b) 120 min. The scale bar is 500 µm. *Reprinted with permission from Ref. [121]. Copyright (2006) Elsevier.*

conventional light microscopy and CM in the *in vitro* and *in vivo* characterization of biomaterials will be discussed in more detail in Chapters 5 and 6.

4.10. SCANNING ELECTRON MICROSCOPY

Scanning electron microscopy (SEM) is an electron microscopic technique that images a sample surface by scanning a focused energetic electron beam. SEM is one of the most common tools to study surface morphology and identify small areas that cannot be resolved by optical microscopy. The primary electrons interact with atoms in the sample surface and various signals are emitted. The primary electrons are emitted from an electron gun. The common types are

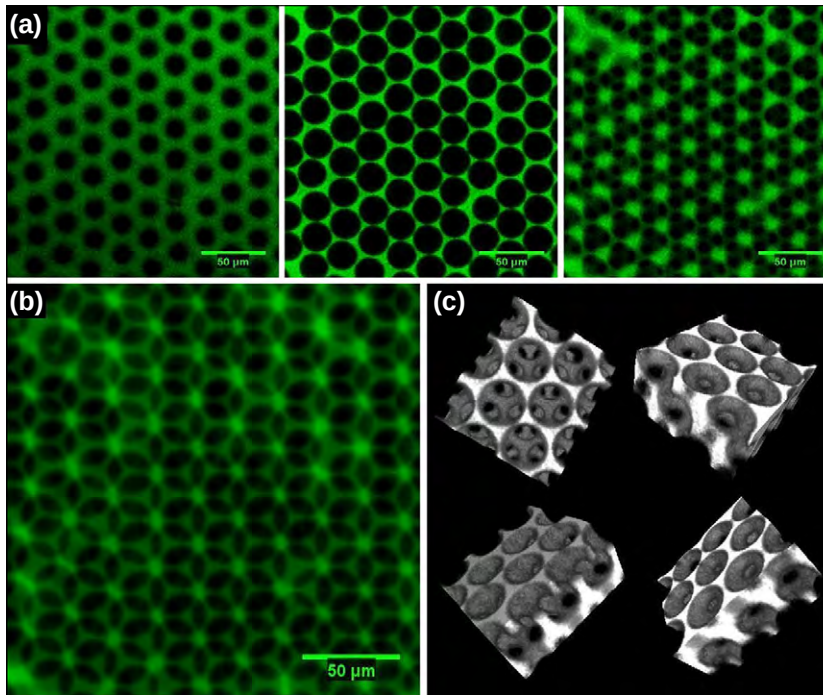

FIGURE 4.25 Images obtained from a confocal image stack of a periodic hydrogel scaffold before annealing: (a) Images showing the surface, the middle of the first layer and the pores between the first and second layer of the scaffold, (b) Z-projection of the three first layers of the scaffold, and (c) three-dimensional reconstruction of a scaffold segment. *Reprinted with permission from Ref. [128]. Copyright (2010) Elsevier.*

thermionic electron emitters as tungsten filament cathodes and lanthanum hexaboride cathodes and field emission sources such as a cold-cathode type using a tungsten single crystal emitter or thermally assisted Schottky type emitter of zirconium oxide. The electrons are typically accelerated to energy of 0.2 keV–40 keV and spatially focused by one or two condenser lenses to a spot about 0.4 nm–5 nm in diameter. The electron beam then passes through scanning coils or deflector plates in the electron column to achieve deflection in the x and y directions for scanning. The scanned area is usually square of rectangle. When the primary electrons strike the sample, the electrons lose energy by repeated random scattering and absorption within a volume of the specimen known as the interaction volume, which resembles a tear drop or balloon with a depth of 1–5 µm into the surface depending on the electron energy. Various signals originate from different depths of the interaction volume and secondary electrons are emitted from the top 5–10 nm of the sample surface and contain topographical information. In addition, reflection of

high-energy electrons by elastic scattering and emission of electromagnetic radiation are some of the phenomena. The emitted signals are detected by specialized detectors and the signals are amplified and displayed on a cathode ray tube (CRT). The CRT display is synchronized with the rastering of the electron beam and the resulting image represents an intensity map of signals emitted within the scanned area.

4.10.1. Secondary Electron Imaging

There are several SEM imaging modes according to the signals detected. Among these modes, secondary electron imaging is the most common. Secondary electrons are low-energy electrons (<50 eV) ejected from atoms via inelastic scattering. As aforementioned, they originate within a few nanometres of the surface due to their low energy. Secondary electrons are detected by an Everhart–Thornley detector which is a type of the scintillator–photomultiplier system. After being attracted towards an electrically biased grid at about +400 V, the secondary electrons emitted are further accelerated towards a scintillator positively biased to about +2000 V and causing the scintillator to emit flashes of light. These electrical signals are amplified by a connected photomultiplier and displayed as a two-dimensional intensity distribution that can be viewed on an analogue video display and saved as a digital image. The brightness of the signal depends on the number of secondary electrons reaching the detector and is sensitive to the surface topography of the sample. For instance, as the electron beam enters the sample perpendicular to the surface, the activated region is uniform about the axis of the beam and a certain number of electrons 'escape' from within the sample. When the angle of incidence increases, the 'escape' distance of one side of the beam will decrease, and more secondary electrons will be emitted. Consequently, steep surfaces and edges of the samples tend to be brighter than flat surfaces in the second electrons images, which results in images with a well-defined, three-dimensional appearance.

Secondary electron imaging is very useful in examining surface topography with high spatial resolution. Topographical images with resolution of <1 nm can even be obtained [130]. However, such high spatial resolution is uncommon for biomaterials as images with this resolution are hard to get and most biomaterials have topographical features larger than 1 nm. There have been many reports on the characterization of biomaterials by secondary electron imaging [131–137]. For instance, Park et al. [131] generated titania (TiO_2) nanotubes with defined diameters between 15 and 100 nm on titanium to direct different behavior of mesenchymal stem cells. The diameters and topographies of various TiO_2 nanotubes were determined by the secondary electron imaging. Rujitanaroj et al. [133] encapsulated small-interfering RNA (siRNA) and transfection reagent (TKO) complexes within nanofibers comprising a copolymer of caprolactone and ethyl ethylene phosphate (PCLEEP) to control the release of siRNA complexes in long-term gene-silencing applications. The

secondary electron images reveal that the SiRNA-encapsulated PCLEEP fiber are successfully fabricated and both the siRNA- and GAPDH siRNA/TKO-encapsulated nanofibers are uniform and bead-free. He et al. [134] fabricated mineralized nanofibrous poly (L-lactic acid) (PLLA) scaffolds for bone regeneration by depositing calcium phosphate on the PLLA scaffolds using an electrodeposition process. As shown in the SEM images in Fig. 4.26, by varying the voltage in electrodeposition, the surface topography of the calcium phosphate coatings on the nanofibrous PLLA scaffolds is quite different. Flower-like topography, flake-like structure, and fiber-like coating are obtained by electrodeposition at 2, 3, and 5 V, respectively. Secondary electrons imaging is also widely used in the *in vitro* characterization of biomaterials after cell seeding [138–140] and more details on secondary electron imaging can be found in Chapter 5.

4.10.2. Backscattered Electron Imaging

Besides secondary electrons, backscattered electrons produced by the electron beam can be used to image the sample surface for a different purpose. Backscattered electrons consist of high-energy electrons, which are reflected or back-scattered out of the specimen interaction volume by elastic scattering with the substrate atoms. Since heavy elements (high atomic number) backscatter electrons more efficiently than light elements (low atomic number), the signal is higher and the spot looks brighter in the image. Hence, backscattered electrons are usually used to monitor the contrast among areas with different chemical compositions. The detector for backscattered electrons is different from that of secondary electrons as the backscattered electrons have high energy (in keV) and the positively biased detection grid has little ability to attract them. The detector used for secondary electron detection is normally positioned on one side of the specimen and is inefficient in the detection of backscattered electrons because few such electrons are emitted in the solid angle subtended by the detector. Therefore, dedicated backscattered electron detectors are positioned above the sample in a 'doughnut' arrangement concentric with the electron beam in order to maximize the solid angle of collection. When all parts of the detector are used to collect electrons, an atomic number contrast is produced. Furthermore, strong topographic contrast can be produced by collecting backscattered electrons from one side above the specimen using an asymmetrical, directional BSE detector. The resulting contrast appears as illumination of the topography from that side. Semiconductor detectors can be made in radial segments and can be switched in or out to control the type of contrast produced (atomic number contrast or topographic contrast) and directionality.

In most cases, backscattered electrons are used to image biomaterials after implantation. There are reports about the *in vivo* characterization of bone replacement biomaterials by backscattered electron imaging [141–143], and

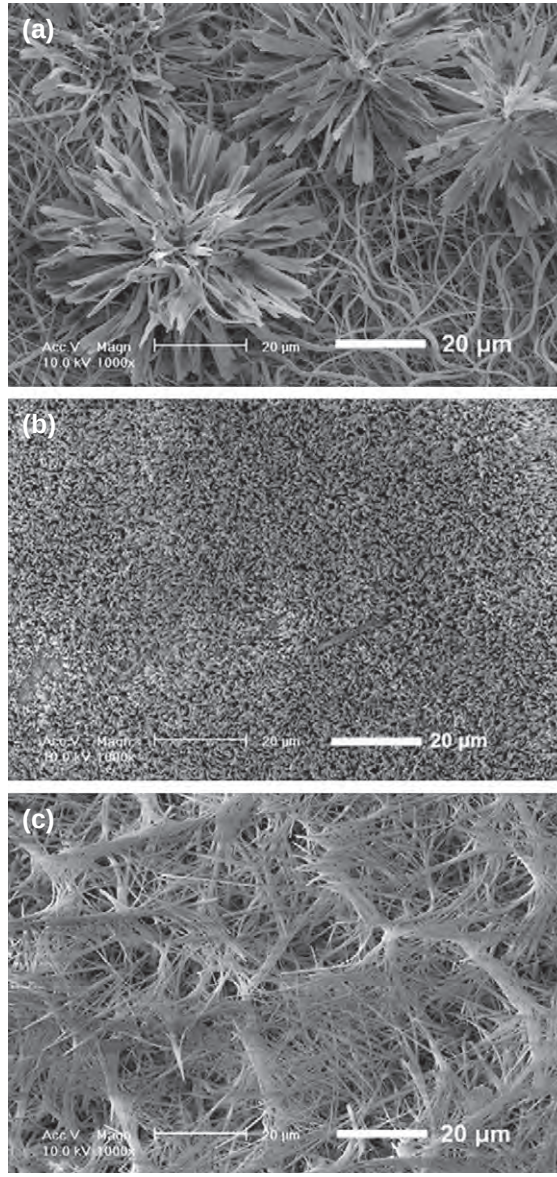

FIGURE 4.26 Secondary electron images of calcium phosphate deposition on electrospun PLLA nanofibrous scaffolds. Electrodeposition is performed for 60 min at 60 °C and (a) 2, (b) 3, and (c) 5 V, respectively. *Reprinted with permission from Ref. [134]. Copyright (2010) John Wiley and Sons.*

the implant materials and newly formed bone can be well differentiated in the images (see Chapter 6 for more details). Before *in vitro* and *in vivo* characterization, backscattered electrons imaging can also be used to characterize the cross-section [144,145] and surface [146,147] of biomaterials by revealing the elemental contrast. Zhang et al. [146] prepared silver-loaded coral hydroxyapatites as bone tissue engineering scaffolds with anti-bacterial properties and observed from the backscattered electron images that silver particles existed on the sample surface, whereas this feature was not observed from the secondary electron images. Variola et al. [147] modified the surface of Ti6Al4V alloy by etching with a H_2SO_4/H_2O_2 solution to improve the surface osteo-compatibility of the sample. The untreated and modified Ti6Al4V alloys were characterized by SEM in the backscattered mode. As shown in Fig. 4.27, the β-phase is initially present as interstitial grains surrounded by α-phase grains in the untreated sample (Fig. 4.27a) and the β-phase grains are preferentially removed in the course of etching (Fig. 4.27b). The resolution of backscattered electron images is not as high as secondary electron ones because the interaction volume for backscattered electrons is much larger than that of secondary electrons.

4.10.3. Energy-Dispersive X-ray Spectroscopy/Wavelength-Dispersive X-ray Spectroscopy

Generally, SEM is equipped with an energy-dispersive X-ray spectroscopy (EDS) and/or wavelength-dispersive X-ray spectroscopy (WDS) detector for elemental analysis or chemical characterization. Both EDS and WDS rely on the detection and investigation of the characteristic X-rays produced by the primary electrons. During electron illumination, an electron in the inner shell of the target atom can be ejected from the shell and an electron hole is created. Subsequently, an electron from an outer shell fills the hole, and the difference in

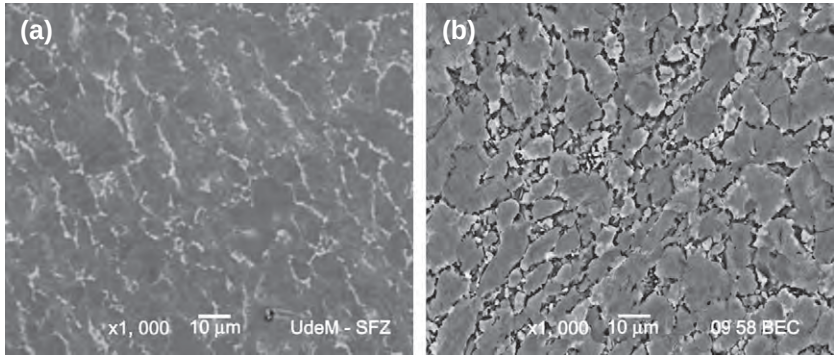

FIGURE 4.27 Backscattered SEM image of (a) polished untreated Ti-alloy disk and (b) the sample after 4 h of exposure to the etching solution. *Reprinted with permission from Ref. [147]. Copyright (2008) Elsevier.*

the energy between the outer- and inner-shell electrons can be released in the form of X-ray [see illustration in Fig. 4.7b]. As the energy of this X-ray is characteristic of the atomic structure of the element from which it is emitted, by measuring the quantity and energy of the X-rays emitted from the sample, the elemental composition of the sample can be determined. WDS differs from EDS in the way the X-ray is detected and that it uses the diffraction patterns created by light–matter interaction as its raw data and the wavelength of the X-ray is calculated by the Bragg' law: $n\lambda = 2d \sin \theta$, where n is an integer, d is the spacing between the planes in the atomic lattice which is known, θ is the measured angle between the incident ray and the scattering planes, and λ is the wavelength of the incident X-ray can be calculated. The spectral resolution of WDS (about 5 eV) is much higher than that of EDS (above 100 eV). However, data collection in WDS is slower than that of EDS as only one element can be monitored at a time in WDS while EDS can gather a spectrum of all the elements in the sample simultaneously.

Characteristic X-rays are not as surface sensitive as secondary electrons because the interaction extent of characteristic X-rays is even larger than that of backscattered electrons. Consequently, as the means for chemical characterization of sample surface, the surface sensitivity of EDS and WDS is not good enough. Nevertheless, EDS is widely used for the elemental analysis of biomaterials 'surface' [148–150] due to the small-area capability. For example, Han et al. [148] synthesized different kinds of calcium hydroxide-loaded biodegradable microcapsules by phase separation and utilized EDS to determine the elemental percentages of the samples. Khaled et al. [150] synthesized strontium-modified titania nanotubes (n-SrO-TiO_2 tubes) by using the alkaline hydrothermal technique and characterized them with EDS mapping. As shown in Fig. 4.28, the elemental maps of the atomic concentrations of Ti, Sr, and O reveal that Ti and Sr are homogeneously dispersed throughout the nanotube samples. It should be noted that there are some limitations in characterizing the sample chemistry with EDS. The first three elements of the periodic table, namely H, He, and Li, do not have enough electrons to produce characteristic X-ray and so they are not detectable by EDS. Furthermore, owing to the low spectral resolution, many elements have overlapping peaks in the EDS spectrum. In spite of the better resolution, WDS is seldom used for biomaterials probably because WDS is not as common as EDS in SEM instruments.

4.10.4. Sample Preparation

Since the typical SEM instrument is under vacuum, the sample is normally required to be dry. To avoid charging, the sample should also be electrically conductive, at least on the surface, and should be properly grounded to prevent accumulation of electrostatic charges on the surface. Metallic samples usually require little special preparation except cleaning and mounting. Non-conductive specimens can charge when bombarded by the electron beam and

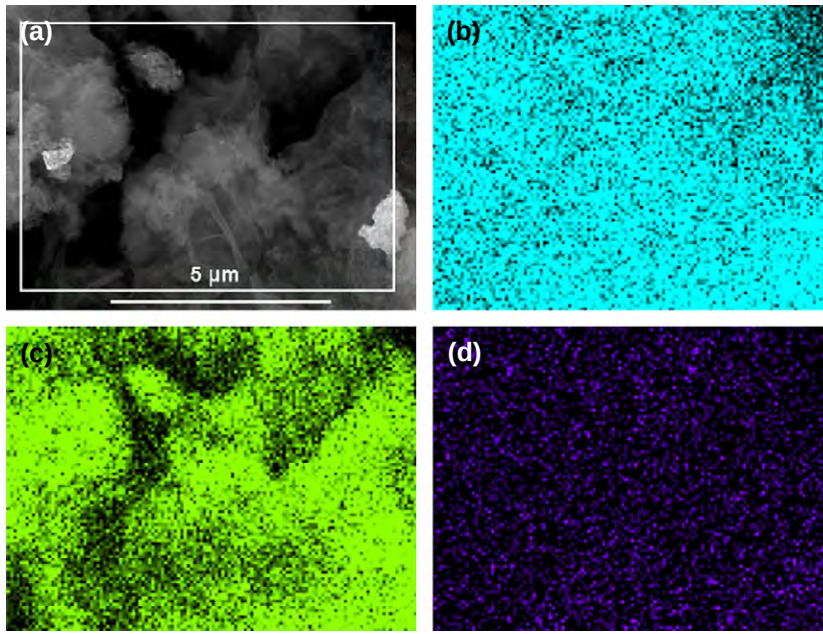

FIGURE 4.28 EDS elemental mapping: (a) Selected area on the sample (*n*-SrO-TiO_2 tubes); (b) Ti mapping; (c) O mapping; (d) Sr mapping. *Reprinted with permission from Ref. [150]. Copyright (2010) Elsevier.*

therefore, they are usually coated with a thin coating of electrically conductive materials such as gold or carbon. Because some biomaterials are hydrated and non-conductive, e.g. hydrogel, before they are inserted into the SEM instrument, a series of pre-treatments such as structure fixing, sample drying, and deposition of a conductive coating are required.

4.10.5. Environmental Scanning Electron Microscopy

Conventional SEM requires samples that are compatible with vacuum conditions. For hydrated and non-conductive biomaterials, the pre-treatments can be complicated and the natural state of the samples may even be altered after the pre-treatments. Environmental scanning electron microscopy (ESEM) [151] has the same working principle as conventional SEM but is specialized for imaging hydrated and non-conductive biomaterials in their natural states. There are differential pumping systems in ESEM instruments, which allow the transfer of the electron beam from the high vacuum part in the gun area to the high-pressure region in the specimen chamber. By placing the sample in the high-pressure specimen chamber where the working distance is short, the

electron beam can produce various signals such as secondary electrons, backscattered electrons, and characteristic X-rays from the sample. Although the signals used in ESEM are the same as those in conventional SEM, the detectors are quite different. A gas detection device is specially designed for the detection of signals in the gaseous environment of ESEM.

Compared to conventional SEM, ESEM boasts several advantages in biomaterials characterization. First of all, hydrated biomaterials can be examined naturally in ESEM, whereas in conventional SEM, the specimens are normally desiccated under the vacuum conditions. Secondly, accumulation of electric charges on the surface of non-conductive specimens can be avoided in ESEM because positively charged ions generated by beam interactions with the gas help to neutralize the negative charges on the specimen surface. In conventional SEM, the insulating specimens without conductive coating will charge up during electron bombardment making imaging problematic or even impossible. Accordingly, hydrated and non-conductive biomaterials can be examined faster and more easily by ESEM as the complex and time-consuming pre-treatments can be avoided. More importantly, the natural surface of the specimens can be imaged by ESEM. Hence, ESEM is widely used for the surface topographical characterization of the hydrated or/and non-conductive biomaterials such as hydrogels [152,153], micelles [154,155], nanofibers [156], and so on. For instance, Fundueanu et al. [152] functionalized the pullulan microspheres (hydrogel) with pendant thermosensitive units to serve as the carriers for drug control and release. ESEM was subsequently used to characterize the extension and collapse of the pendant thermosensitive units below and above the lower critical solution temperature. Shi et al. [156] synthesized the copolymer (PLA-co-MPC) of L-lactide with a monomer containing propargyl group and then electrospun it into nanofibers for proteins immobilization. The natural morphology of the PLA-co-MPC nanofibers was evaluated by ESEM, which indicates that the nanofibers are smooth and continuous with a diameter of 2–4 μm (Fig. 4.29). Backscattered electrons [157] and

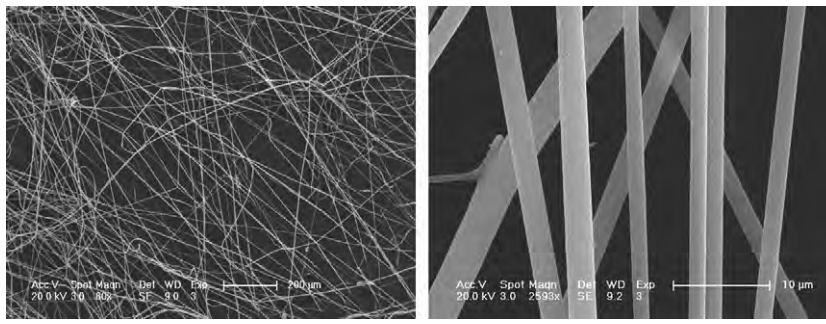

FIGURE 4.29 ESEM images of the electron-spun PLA-co-MPC nanofibers. *Reprinted with permission from Ref. [156]. Copyright (2008) Elsevier.*

characteristic X-rays [158] in ESEM can also be used for the characterization of biomaterials.

However, there are some disadvantages of ESEM. The main one arises from the limitation of the distance in the specimen chamber (1–10 mm) over which the electron beam remains usable in the gaseous environment. The presence of gas may cause unwanted effects in certain applications and the mechanism of these side-effects is not always clear.

In summary, SEM is a widely used tool in the characterization of biomaterials. Various signals such as secondary electrons, backscattered electrons, and characteristic X-rays emitted from the sample surface can be used to determine different properties of the samples including surface topography and elemental distributions. However, because of the vacuum conditions in conventional SEM, hydrated and/or non-conductive biomaterials must be pre-treated and the process can be complicated and sometimes destructive. Hence, for these biomaterials, ESEM is preferable as the complex and time-consuming pre-treatments are avoided and the samples can be imaged in their natural state. Owing to space limitation, we only describe selected examples before *in vitro* and *in vivo* experiments in this chapter. The *in vitro* and *in vivo* characterization of biomaterials by SEM will be discussed in more detail in the following chapters (see Chapters 5 and 6).

4.11. SCANNING TUNNELLING MICROSCOPY AND ATOMIC FORCE MICROSCOPY

Scanning probe microscopy (SPM), which was adopted with the invention of the scanning tunnelling microscopy (STM) in 1981, encompasses a family of microscopic techniques that image surfaces with a physical probe that scans the specimen. An image of the surface is obtained by mechanically scanning the probe line by line and recording the probe–surface interaction as a function of position. Among the various surface imaging techniques, SPM has the advantages of easy sample preparation, operation in a liquid environment, and particularly high spatial resolution. Depending on the sample, individual atoms can even be imaged by SPM. According to the different probe–surface interactions, SPM is classified into various sub-types such as STM, AFM, frictional force microscopy, and so on. Of these techniques, STM and AFM are most commonly used for the evaluation of sample surface morphology.

4.11.1. Scanning Tunnelling Microscopy

STM is based on the concept of quantum tunnelling. When a conducting tip is brought very close to the surface to be examined, a bias (voltage difference) allows electrons to tunnel through the gap in between and the resulting tunnelling current is a function of the tip position, applied voltage, and local density of states on the sample surface. Lateral information is acquired by

monitoring the current as a function of the tip position during scanning across the surface. Since the tunnelling current varies exponentially upon the separation between the STM tip and sample surface, a vertical resolution of 0.01 Å with a lateral resolution of 0.1 Å is attainable by STM for electronically inhomogeneous surfaces. However, the STM image obtained, even at atomic resolution, is far from being a simple visual representation of the spatial locations of atoms. Instead, it is a complex image determined by a convolution of the electronic structures of the tip and the sample surface. Only for surfaces which have relatively uniform electronic properties (and with dimensions $>$10 Å), the STM image can effectively represents the surface topography.

Despite the outstanding spatial resolution of STM, publications about the use of STM in biomaterials characterization are few and only related to selective substrates such as gold [159,160] and carbon [161] because of practical obstacles. First and mainly, the samples for STM measurement should be conductive, but many biomaterials are organic or inorganic non-metallic materials which are insulating. Even for metallic biomaterials such as titanium, the surface usually has a native oxide which is too thick for electron tunnelling. Second, STM is a tool to determine the surface electronic structure. The image contrast does not necessarily bear a simple relationship with surface topography, and interpretation of STM images may not be straightforward. Although the application of STM to biomaterials is limited at present, STM is the preferred method to investigate the atomic structures of the novel conductive materials such as carbon nanotubes [162,163], silicon nanowires [164], and graphene [165,166] and more applications are being discovered.

4.11.2. Atomic Force Microscopy

At high tunnelling currents, the STM tip may interact physically with the surface in such a way that disruption of the surface structure occurs. In fact, there is usually a finite interaction force between the tip and sample surface and even at relatively low tunnelling currents, the interaction force may be substantial when measured against the strengths of molecular interactions. Consequently, Binnig et al. [167] invented the first atomic force microscope in 1986 and 3 years later, the first commercial atomic force microscope became available.

A commercial AFM instrument consists of a cantilever with a sharp tip (probe) at its end that is used to scan the specimen surface. The cantilever is typically made of silicon or silicon nitride (100–200 μm long and about 1 μm thick) with a tip radius of curvature on the order of nanometres. When the tip is brought close to the sample surface, the force between the tip and sample leads to a deflection of the cantilever according to Hooke's law. The deflection is measured using a laser reflected from the top surface of the cantilever into an array of photodiodes. A schematic diagram of a typical AFM instrument is depicted in Fig. 4.30. There are other AFM methods available involving optical interferometry, capacitive sensing, and piezoresistive AFM cantilevers.

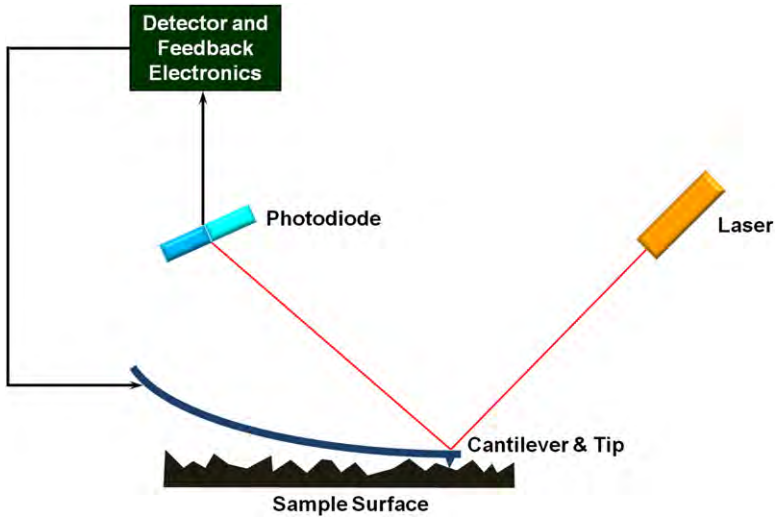

FIGURE 4.30 Schematic diagram of a typical commercial AFM instrument.

Depending on the information sought, the force measured in AFM can be different and it includes mechanical contact force, van der Waals force, capillary force, chemical bonding, electrostatic force, magnetic force, and so on.

Despite the short history, AFM has become one of the essential tools for surface imaging, particularly on the nanoscale. With regard to biomaterials, AFM boasts some advantages in comparison with other imaging techniques. Sample preparation for AFM is substantially simpler than that required by SEM or TEM and AFM can produce detailed three-dimensional maps rather than two-dimensional images without expensive and time-consuming sample preparation. For non-conducting samples, AFM can provide a direct view of surface features in high resolution, whereas in SEM, a conductive coating is needed and it may hide some surface details and even damage or alter the surface features. Furthermore, a vacuum is not required and samples can be imaged in ambient air or liquid. These advantages have rendered AFM suitable for biomaterials research in the native or quasi-native environment as well as in real time.

There are three common modes of AFM: contact mode, non-contact mode, and tapping mode. In the contact mode, the AFM tip scans across a surface at a very low force and is deflected by the repulsive force between the tip and surface atoms. A feedback loop maintains constant deflection of the cantilever by vertically moving the scanner as it scans laterally across the surface and then the topographic image of the sample surface is constructed. As the tip always

exerts a mechanical load on the sample which may lead to damage, contact AFM is not suitable for soft biomaterials.

In the non-contact mode, the tip of the cantilever does not make direct contact with the sample surface. Instead, the cantilever is oscillated at a frequency slightly above its resonant frequency where the amplitude of oscillation is typically a few nanometres (<10 nm). The van der Waals force, which is strongest from 1 nm to 10 nm above the surface, or any other long-range force which extends above the surface decreases the resonance frequency of the cantilever. This decrease in resonant frequency combined with the feedback loop system maintains a constant oscillation amplitude or frequency by adjusting the average tip-to-sample distance. In measuring soft samples, non-contact AFM is preferable over contact AFM as it does not suffer from tip or sample degradation effects that are sometimes observed with contact AFM. However, non-contact AFM is also not commonly used for biomaterials because most biomaterials are hydrophilic and develop a liquid meniscus layer under ambient conditions. Keeping the probe tip close enough to these samples may possibly lead to the tip sticking resulting in low-resolution imaging.

In the tapping mode, also called intermittent contact mode, the cantilever is driven to oscillate up and down at near its resonant frequency similar to that in the non-contact mode. However, the amplitude of this oscillation is much greater than 10 nm, typically 100–200 nm. Owing to the force (van der Waals force, electrostatic force, etc.) acting on the cantilever when the tip comes close to the surface, the amplitude of this oscillation is decreased as the tip gets closer to the sample. As the cantilever is scanned over the sample, an electronic servo adjusts the height of the cantilever to maintain constant oscillation amplitude or frequency. Among the three AFM modes described here, tapping-mode AFM is the most widely used in biomaterials characterization. In tapping mode AFM, although there is still mechanical contact, damage to the sample surface is lessened as the contact is intermittent and no lateral frictional force is applied to the sample. Tapping-mode AFM is even gentle enough for the visualization of supported lipid monolayers under liquid medium [168]. Moreover, the problem of non-contact AFM in hydrophilic biomaterials characterization can be effectively avoided.

Tapping-mode AFM can provide topographical information with superior resolution on soft biomaterials such as biopolymers. In a typical example reported by Zhou et al. [169], tapping mode AFM was performed to acquire the height image of self-assembled peptide-based hydrogels in high resolution. Besides the height images, the phase images were also obtained in the tapping mode simultaneously. The z-scale of the phase images was in degree (°), which is quite different from that of the height images. In phase imaging, the phase lag between the driving oscillation and cantilever response is measured. The magnitude of this lag provides an indication of the amount of energy dissipated in the tip–sample interaction, which is related to the surface mechanical

properties of the sample. Therefore, phase imaging can be used to determine the size, shape, and spacing of different materials domains that cannot otherwise be discerned from heights alone. Many types of biomaterials are modified to produce heterogeneous surface properties and so, phase imaging is a useful tool [170–173]. For example, Ye et al. [170] fabricated self-assembled RADA16-I peptide on mica at different pH values (pH = 1 or 4) in peptide solutions and investigated the samples by tapping-mode AFM. The height and phase images are depicted together in Fig. 4.31. The nanofibers produced at pH = 1 (Fig. 4.31D) are branched, whereas the nanofibers formed at pH = 4

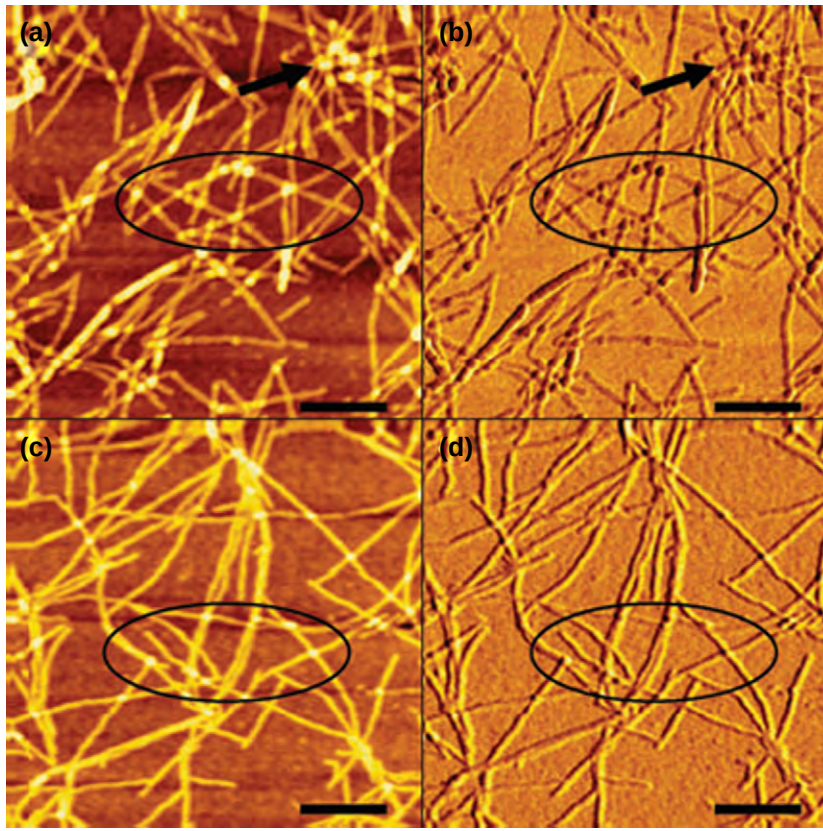

FIGURE 4.31 Typical AFM morphological images and corresponding phase images of self-assembling peptide RADA16-I denatured at pH = 4 and 1 on a freshly cleaved mica surface. After denaturing at pH = 4, the height image (a) with the maximum 3.0 nm scale and the phase image (b), with the maximum 7° scale. At pH = 1, the height image (c) with the maximum 2.6 nm scale and the phase image (d) with the maximum 0.9° scale. The scale bar is 500 nm. *Reprinted with permission from Ref. [170]. Copyright (2010) John Wiley and Sons.*

have no branch (Fig. 4.31B), although these features are not so clear in the corresponding height images (Fig. 4.31A and C).

In some situations, contact-mode AFM is used to study biomaterials, particularly when the lateral force images are desired. Lateral force images, also called friction images, map the lateral bending of the cantilever in the contact mode. The signals measured are closely related to the frictional interaction between the tip and the sample and so are useful in the identification of chemical differences on the samples. Similar to phase images in the tapping mode, lateral force images can be obtained together with height images simultaneously while the unit of *z*-scale is volt (V). There have been studies on the use of lateral force imaging to probe the chemical functionalities of potential biomaterials [174–176]. For example, Denis et al. [175] fabricated samples with a monolayer of CH_3-terminated alkylsilanes in nanoscale tracks surrounded by a monolayer of PEG-terminated alkylsilanes (named as CH_3-*X*/PEG-*Y*, *X* and *Y* are the widths of the CH_3 and PEG tracks in nanometres, respectively). These chemical nanopatterns were quite different in collagen adsorption and could lead to collagen nanopatterns on them by solution immersion. Figure 4.32 presents the height (a) and lateral force (b and c) AFM images obtained on sample CH_3-50/PEG-550 before collagen adsorption. The lateral force images show strong contrast between the tracks and matrix when the topographical image obtained is smooth along the *z*-scale (10 nm). The reversal of forward and backward lateral force images evidently indicates that sample CH_3-50/PEG-550 is chemically anisotropic.

Besides sample imaging, commercial AFM apparatus can be used to characterize the mechanical properties where the AFM tip serves as an indenter. This technique is called AFM indentation. When the indenter is pressed against the sample surface, load versus displacement curves are acquired. Since the load is applied by the cantilever, only mechanical characterization of compliant samples is allowed. In contrary, for stiff materials, the cantilever is more easily deflected than indenting the sample surface. Thus, this AFM-based technique can be applied to compliant biomaterials such as biopolymers. The force–displacement curves can even be used to evaluate the elasticity (resilience) of the substrates by converting them into force–penetration/retraction curves and calculating the area ratio of penetration curve to retraction curve [177,178].

There are other AFM-related techniques for biomaterials characterization. With magnetic or acoustic accessories, more details about the materials properties can be obtained. A typical example was presented by Block et al. [179] who suggested a new approach (called nanoparticle identification on magnetic imaging atomic force microscopy, NIOMI AFM), which was capable of distinguishing superparamagnetic maghemite and diamagnetic gold nanoparticles from a mixture by means of the magnetic interactions. As shown in Fig. 4.33, it is impossible to differentiate both types of nanoparticles by only relying on the information provided by the height map (Fig. 4.33 (top)).

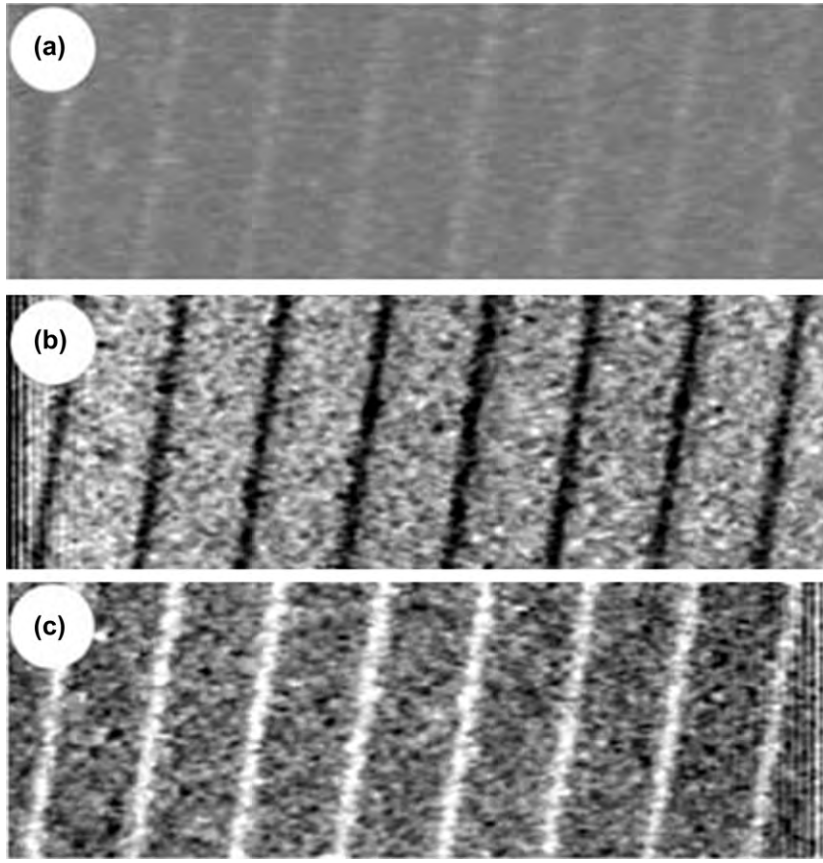

FIGURE 4.32 AFM height image (a; z range: 10 nm) and lateral force images (b, c; z range: 0.3 V) simultaneously recorded by forward (a, b) or backward (c) scanning of a CH_3-50/PEG-550 area ($5 \times 1.7\ \mu m^2$) in air. *Reprinted with permission from Ref. [175]. Copyright (2005) John Wiley and Sons.*

However, in the amplitude map created by NIOMI AFM, the maghemite and gold nanoparticles exhibit different contrast (Fig. 4.33 (middle)) and they are easily distinguished (Fig. 4.33 (bottom)). NIOMI AFM can even be used to characterize biofunctionalized nanoparticles (protein-tagged maghemite nanoparticles) [179]. The AFM tip can also be functionalized by protein adsorption or chemical covalent bonding and this AFM approach is called chemical force microscopy. Interested readers are referred to a review [180] for more details. Furthermore, AFM is a powerful tool for the *in vitro* characterization of biomaterials (mapping cells, viruses even their proteins) and this topic will be discussed in detail in Chapter 5.

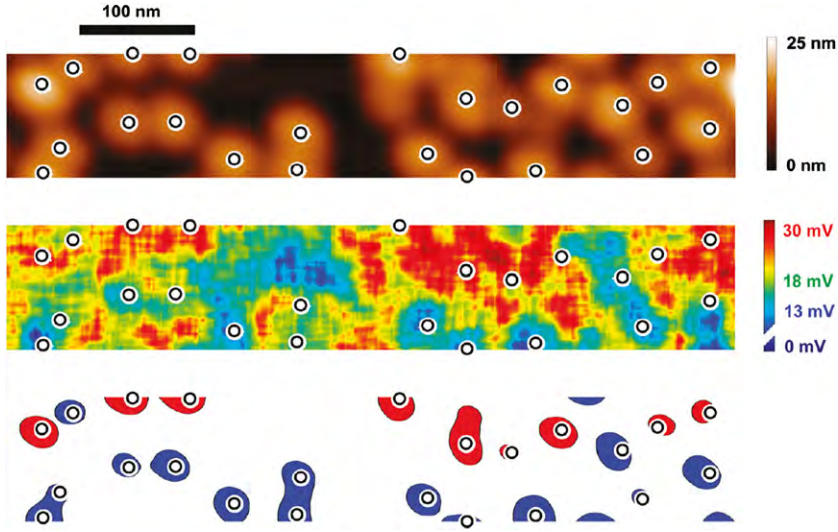

FIGURE 4.33 NIOMI AFM imaging of a sample containing superparamagnetic maghemite and diamagnetic gold nanoparticles. Image size, 110 × 640 nm^2; top, height profile; middle, amplitude map of the AFM cantilever oscillation (after line wise flattening and low pass filtering for noise reduction); bottom, correlation of height and amplitude map for nanoparticle identification (diamagnetic nanoparticles are marked in blue, while red color is used for the superparamagnetic ones). The centers of the particles are recognized by an algorithm in the height map (top, monochrome circles) and then transferred to the amplitude map for comparison. Correlation of the nanoparticle position with the color in the amplitude map identifies the nanoparticle upon their magnetization (cf. bottom). *Reprinted with permission from Ref. [179]. Copyright (2011) American Chemical Society.*

4.12. PROFILOMETRY

Profilometer, which is historically similar to the classical phonograph, is used to determine the surface topography of a solid sample. By tracking the surface changes using a profilometer, the surface roughness and morphological images of the samples can be determined. Modern profilometers can be roughly classified as contact profilometers and non-contact profilometers. Generally, contact profilometry is similar to contact-mode AFM, except that the measurement range is wider and the spatial resolution is lower. In contact profilometry, a stylus typically made of diamond vertically in contact with a sample is moved laterally across the sample surface for a specified distance at a specified contact force. The surface variations as monitored by the vertical stylus displacements are measured as a function of position to obtain the profile of the sample surface. Contact profilometry is a direct technique as no modelling is required. The stylus tip can be as small as 20 nm and so the lateral resolution is much better than that of white-light optical profilometry (the

resolution of optical profilometry is determined by the optical wavelength). More importantly, compared to optical profilometry, this method is less affected by contaminants on the sample surface and it is more preferable than optical profilometry when the measurement environment is complex. Contact profilometry is widely used to study biomaterials [97,181–183]. For instance, Sima et al. [181] formed fibronectin layers on a silicon substrate and utilized contact profilometry to measure the profile of the layers. Saber-Samandari et al. [97] deposited calcium phosphate on titanium by thermal printing and conducted contact profilometry to determine the profiles of the deposits. Barranco et al. [183] fabricated oxide barriers on biomedical Ti6Al4V by blasting with different particles and thermal treatment. Contact profilometry was subsequently performed to determine the roughness of the samples.

As an alternative to stylus-based profilometry, optical profilometry is a non-contact method that can provide similar information as contact profilometry. There are also advantages associated with optical profilometry such as high vertical resolution and convenient operation. A big advantage of this method is that it is a non-contact technique and hence, the instrument and samples cannot be damaged by surface wear or careless operators. Optical profilometry is also commonly used to measure the surface topography of biomaterials [184–186]. Park et al. [184] modified Ti–6Al–4V alloys by a hydrothermal treatment in a strontium-containing solution and used optical profilometry to determine the surface roughness of the modified samples. Truong et al. [186] achieved ultrafine crystallinity in the bulk of titanium by severe plastic deformation by means of equal channel angular pressing (ECAP). By means of optical profilometry, the surface roughness and the topographical image of polished ECAP-Ti were obtained. Besides measuring the surface profiles, roughness, and topography, profilometry can even be used to determine the thickness [187] and wear depth [188] of biomaterials, and interested readers are referred to the cited articles for more information.

4.13. CONTACT ANGLE MEASUREMENT

Contact angle (CA) measurement is a commonly used thermodynamic method for the characterization of surface hydrophilicity/hydrophobicity of biomaterials. As perhaps one of the oldest methods used to investigate biomaterials surfaces, it yields very useful information as the surface hydrophilicity of biomaterials is crucial to the functions of biomaterials such as cell adhesion and spreading. CA measurement is a relatively simple method for solid samples and typically no special sample preparation is required. Anyway, the samples characterized should be clean enough and do not swell or dissolve in the test liquid. For an immobile surface, CA measurement is very surface method as the CA is only related to the outermost 3–10 Å of the surface. There are several types of CA measurements and the more common Wilhelmy method, sessile drop method, and captive bubble method are described here.

4.13.1. Wilhelmy Method

Wilhelmy method is a dynamic method by measuring the equilibrium surface or interfacial tension at the air–liquid or liquid–liquid interface. In this method, the solid sample has same properties on both sides and is oriented perpendicularly to the interface. The wetting force on the solid is measured as the solid is immersed in or withdrawn from a liquid of a known surface tension. The average advancing and receding CAs (θ) is calculated according to the equation:

$$\cos\theta = (F - F_b)/I\sigma,$$

where F is the total force measured by the force metre, F_b is the force of buoyancy due to the solid sample displacing the liquid, I is the wetted length, and σ is the known surface tension (force per unit length) of the liquid.

As a lot of modern biomaterials are surface modified to obtain different properties on both sides, the Wilhelmy method is not a popular tool. However, there is a key advantage in that the Wilhelmy method is not limited by the sample size and shape and so single fiber can be used to determine the CAs [189,190]. The Wilhelmy method can even be adopted on the nanoscale by making use of a nanotube [191] or AFM probe [192,193] as the cantilever to measure the wetting forces of nanotubes and nanofibers. Hence, the Wilhelmy method will attract more attention in the future as more biomaterials have a small size.

4.13.2. Sessile Drop Method

There are two kinds of sessile drop method, namely the static sessile drop method and dynamic sessile drop method. In the static sessile drop method, a droplet of pure liquid is deposited vertically onto the sample surface and CAs are measured by a CA goniometer using an optical sub-system. The angle formed between the solid/liquid interface and liquid/gas interface is determined as the liquid CA (Fig. 4.34). The dynamic sessile drop method is similar to the static sessile drop method but requires the drop to be modified. Both advancing angle (the largest CA possible without increasing its solid/liquid interfacial area by adding volume dynamically) and receding angle (the smallest possible angle by removing the volume without decreasing its solid/liquid interfacial area) are measured in the dynamic sessile drop method. The difference between the advancing and receding angle is the CA hysteresis. The advancing and receding angle determined by the dynamic sessile drop method can also be used to calculate the equilibrium CA [194,195].

The sessile drop method is the most commonly used CA measurement for biomaterials [196–199] because it is a straightforward approach revealing surface energetics of the samples. Typically, pure water serves as the test liquid. For instance, Yamanlar et al. [196] described a simple approach to functionalize

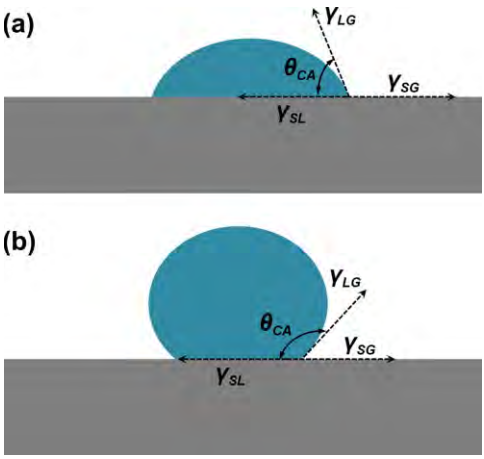

FIGURE 4.34 Illustration of the sessile drop method by a solid substrate with good wettability (a) or poor wettability (b). θ_{CA} is the liquid contact angle, and γ_{SL}, γ_{SG}, and γ_{LG} represent the solid/liquid, solid/gas, and liquid/gas interfaces, respectively.

photo-cross-linked HA hydrogels by deposition of poly(L-lysine) (PLL) and HA multilayer films layer by layer (LBL). After each layer deposition, they measured the water CA on the substrate using the static sessile drop method and the results directly indicate that HA reduce the CA, whereas PLL layer increases the CA on the HA hydrogel surface in an alternating manner. Alauzun et al. [197] covalently linked hyaluronic acid (HA) to biomedical PDMS elastomer surfaces using a series of steps to achieve better biocompatibility and used the dynamic sessile drop method to characterize the hydrophilicity. The results reveal that both the advancing water CA and receding water CA are reduced after each step of chemical modification.

Besides the surface chemistry, the surface roughness is also crucial to the CA in the sessile drop method [200]. When the liquid and rough substrate are in a wetted contact (liquid completely fills the grooves of the rough surface where they contact), the Wenzel's theory provides correlation between the surface roughness and the apparent CA of liquid droplet with the following relationship:

$$\cos\theta_{\mathrm{w}} = r\cos\theta,$$

where θ_{w} is the apparent CA in the Wenzel mode, θ is the true CA, and r is the surface roughness factor. As the roughness factor (r) is always above 1, if the CA of a liquid on a smooth surface is less than 90°, the apparent angle on a rough surface will be smaller, whereas for a true CA $> 90°$, the CA on a rough surface will be larger. In other words, in the Wenzel mode, there is an amplified effect of surface roughness to the CA (for $\theta < 90°$, $\theta_{\mathrm{w}} < \theta$; for $\theta > 90°$, $\theta_{\mathrm{w}} > \theta$). Another theory, Cassie's theory, is applicable when the liquid and rough substrate are in non-wetted contact (vapour pockets are assumed to be trapped underneath the liquid). In the Cassie mode, the apparent CA is always larger than the true CA, no matter whether the true CA is above 90° or not.

For solid biomaterials with surface micro-/nano-structures, the sessile drop method can be used to characterize the hydrophilicity and hydrophobicity when the surface roughness is taken into consideration [98,201–203]. Ma et al. [201] prepared polyethylene terephthalate (PET) nanofibers by electrospinning and modified the surface with polymerization of methacrylic acid (PMMA) grafting followed by gelatin grafting to achieve better surface biocompatibility. Both the static and dynamic sessile drop methods were employed to characterize the wettability of PET nanofibers before and after surface modification. The PET films before and after PMMA and gelatin grafting were also analyzed and compared to PET nanofibers. As shown in Table 4.1, the PET nanofibers are totally different from the PET films based on the water CAs. The original PET nanofibers have the much higher advancing and static water CAs than the original PET film, whereas the receding angle is much smaller. Both PMMA and gelatin modification enhance the hydrophilicity of the PET surface. The decrease in the water CA is much more significant on the PET nanofibers due to its surface structure. According to the theories described above, the water CA on the original PET nanofibers is in the Cassie's mode (air is trapped in the pores and the CA appearance is larger than the true CA). With regard to the PET nanofibers after PMMA and gelatin grafting, the apparent water CA is changed to the Wenzel's mode (true CA is $<90^\circ$ and apparent CA is even smaller as water is sucked into the nanofibers).

By using this method, the surface energy of the solid biomaterials can be calculated when the surface energy of the test liquid is known and the liquid-sample CAs are measured. Generally, the use of different test liquids is required to calculate the surface energy. The surface energy has the unit of Joules per area, which is equivalent to that in the case of liquids that surface tension is

TABLE 4.1 Water Contact Angles of the Original and Surface-modified PET Films and PET nanofibers

Sample	Advancing (deg)	Receding (deg)	Static (deg)
Original PET films	97 ± 3	53 ± 4	80 ± 2
PMAA-grafted PET films	74 ± 2	19 ± 1	53 ± 2
Gelatin-grafted PET films	71 ± 3	17 ± 2	50 ± 3
Original PET nanofibers	144 ± 3	15 ± 2	128 ± 3
PMAA-grafted PET nanofibers	–	–	0
Gelatin-grafted PET nanofibers	–	–	0

Reprinted with permission from [201]. Copyright (2005) Elsevier.

measured in Newton per metre. It is known that surface energy can be subdivided according to the various interactions such as interactions due to dispersive (van der Waals) force, hydrogen bonding, polar interactions, acid/base interactions, and so on. Generally, dispersive interactions and polar interactions are the major contributions to the overall surface energy. In this case, the overall surface energy can be described as:

$$\sigma_S = \sigma_S^D + \sigma_S^P \text{ and } \sigma_L = \sigma_L^D + \sigma_L^P,$$

where σ_S is the total surface energy of the solid, σ_S^D and σ_S^P are, respectively, the dispersive and polar components of the solid surface energy, σ_L is the total surface tension/energy of the liquid, and σ_L^D and σ_L^P are, respectively, the dispersive and polar components of the liquid surface energy. Many theories have been employed to determine the surface energy from CAs and they differ in derivation, convention, and number of parameters. The common theories used such as the Owens/Wendt theory [204–207] and the Fowkes theory [208] divide the surface energy into two components: surface energy due to dispersive interactions and surface energy due to polar interactions. The Fowkes theory's principle equation is mathematically equivalent to that of Owens/Wendt:

$$\sigma_L(1 + \cos\theta) = 2(\sigma_S^D)^{1/2}(\sigma_L^D)^{1/2} + 2(\sigma_S^P)^{1/2}(\sigma_L^P)^{1/2}.$$

Thus, by utilizing two test liquids with known surface energies (σ_L^D and σ_L^P) to measure the CAs on a solid sample, the surface energy of the sample (σ_S^D and σ_S^P) can be calculated.

The sessile drop method has advantages and disadvantages. Aside from the straightforward nature, another advantage of the sessile drop method is that with a large-enough solid surface, multiple droplets can be deposited in various locations on the sample to determine the surface heterogeneity. However, when the sample is only large enough for one droplet, the determination of sample's heterogeneity will be difficult. The CA measurement by the sessile drop method is impractical if the sample is even smaller (not large enough for only one droplet). In addition, this measurement is hampered by the inherent subjectivity as the placement of the lines is determined either by the user looking at the picture or by the image analysis software's definition of the lines.

4.13.2.1. Captive Bubble Method

The captive bubble method measures the wettability of samples in a liquid (probably in water). In this method, an air bubble is placed in contact with the sample immersed in a solution. After the contact, the drop profile of the air bubble is imaged using a charge-coupled device (CCD) camera and the CA is calculated from the image. As shown in Fig. 4.35, the interface between the solid sample and droplet is the solid/gas interface. As the CA (liquid, θ_{CA}) is defined as the angle formed between the solid/liquid interface and the liquid/gas interface,

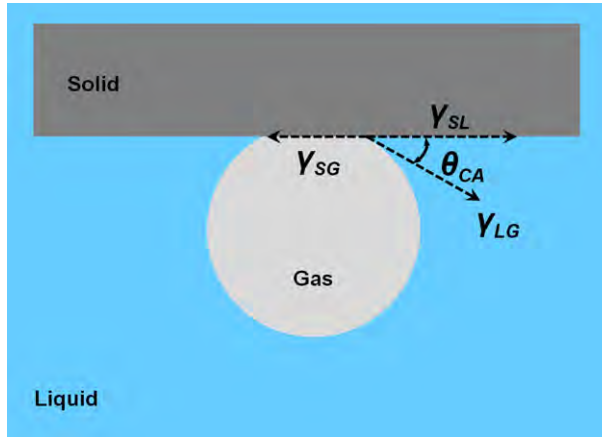

FIGURE 4.35 Illustration of the captive bubble method by a solid substrate with good wettability. θ_{CA} is the liquid contact angle, and γ_{SL}, γ_{SG}, and γ_{LG} represent the solid/liquid, solid/gas, and liquid/gas interfaces, respectively.

the location of θ_{CA} is different from that in the sessile drop method (comparing Fig. 4.35 with Fig. 4.34). The captive bubble method can also be performed in the dynamic mode by using a syringe plunger to increase or decrease the air bubble volume and both the advancing and receding angles can be measured as a result.

Although it is not as popular as sessile drop method, the captive bubble method is useful to the biomaterials with hydrated surfaces [209–212]. For instance, it is good for the investigation of biomedical hydrogels since the materials are immersed in a liquid throughout the process and, therefore, does not undergo dehydration. It has also been pointed out [209,210] that for hydrated surfaces, the water CA measured by the captive bubble method does not agree with that measured by the sessile drop method, probably due to sample dehydration when the sample is exposed in air.

In conclusion, the CA measurement is a useful analytical tool for biomaterials not only revealing the surface energetics but also relating to the surface structure. Comparison of CA measurements on the control and surface-modified biomaterials is usually adopted to confirm successful alteration of the sample surface. Aside from the three types mentioned above, there are other types of CA measurements such as the capillary penetration method but owing to space limitation, they are not described here.

4.14. ELLIPSOMETRY

Ellipsometry is a specular optical technique, which provides unequalled capabilities for thin film metrology. In this technique, electromagnetic radiation is emitted by a light source and linearly polarized by a polarizer, passes through an

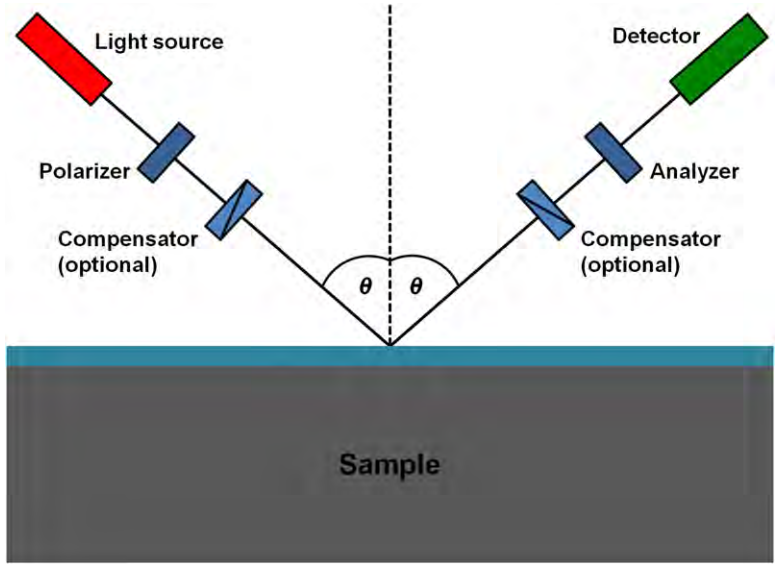

FIGURE 4.36 Schematic diagram of ellipsometry.

optional compensator (retarder, quarter wave plate), and irradiates the sample. After reflection, the radiation passes a compensator (optional) and a second polarizer (analyzer) and is detected. As schematically illustrated in Fig. 4.36, the incident and reflected beams span the plane of incidence. The polarization state of the light incident upon the sample may be decomposed into the *s* and *p* components (the *s* component oscillates perpendicular to the plane of incidence and parallel to the sample surface and the *p* component oscillates parallel to the plane of incidence). The amplitudes of the *s* and *p* components, after reflection and normalized to their initial value, are denoted by r_s and r_p, and are used to calculate the complex reflectance ratio (ρ) by the following equation:

$$\rho = r_p/r_s = \tan(\Psi)e^{i\Delta}$$

where $\tan(\Psi)$ is the amplitude ratio upon reflection, and Δ is the phase shift (difference). By performing a suitable model analysis on the data, Ψ and Δ, which match the experimental data best, are calculated and provide the optical constants and thickness of the sample.

Based on the analysis of the change of polarization of light reflected off a sample, ellipsometry can yield information about layers that are thinner than the wavelength of the probing light itself, even down to a single atomic layer. As an optical technique, the non-destructive and contactless characteristics of ellipsometry are desirable for soft layers on biomaterials. Furthermore, since ellipsometry measures the intensity ratio instead of pure intensity, it is less

affected by intensity instability of the light source or atmospheric absorption, and no reference measurement is necessary thus yielding very good accuracy.

Ellipsometry has many applications in many different fields such as semiconductor physics, microelectronics, biomaterials, and so on. In the biomaterials field, ellipsometry is commonly used to characterize the thickness of biofunctional layers on the substrates ranging from a few Angstroms to several micrometres for layers which are optically homogeneous and isotropic and when a significant refractive index discontinuity exists at the interface. Both monochromatic ellipsometry [213,214] and spectroscopic ellipsometry [215–217] are utilized to determine the thickness of the layers. For instance, Toworfe et al. [213] used monochromatic ellipsometry with a HeNe laser source (632.8 nm) to characterize the thickness and homogeneity of calcium phosphate coated on various surface functionalized oxidized silicon substrates. Pei et al. [217] fabricated surface density gradients of PEG on titanium dioxide surfaces by a controlled dipping process and variable-angle spectroscopic ellipsometry was employed to determine the thickness of the gradient polymer coverage.

Besides conventional characterization of film thickness, ellipsometry can be employed *in situ* (referred to as *in situ* ellipsometry) in dynamic measurements [218–220]. Santonicola et al. [219] grafted polymeric brushes of poly (methacrylic acid) on silicon substrates and then made use of *in situ* ellipsometry to quantify the pH-induced swelling and collapse of the grafted polymer layers in the liquid environment. Blacklock et al. [220] produced the assembly of LBL films on a flexible stainless steel substrate by using plasmid DNA and reducible hyperbranched poly(amido amine) (RHB) polycation. *In situ* ellipsometry was performed subsequently to confirm the disassembly of the films under reducing conditions. As shown in Fig. 4.37, the thickness of the

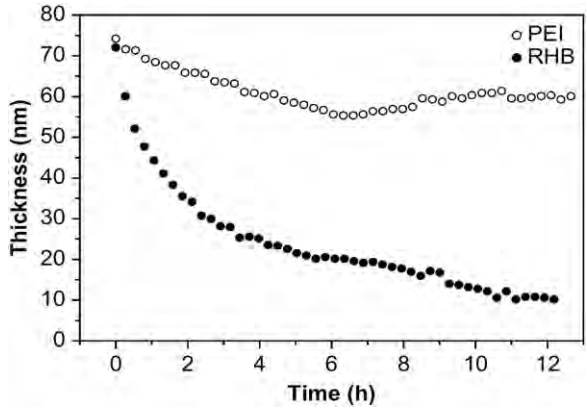

FIGURE 4.37 Film disassembly in reducing conditions. Thickness of $(DNA/RHB)_{15}$ (solid circles) and $(DNA/PEI)_{15}$ (hollow circles) films deposited on the surface of silicon wafer was determined by *in situ* ellipsometry in 20 mM DTT solution. *Reprinted with permission from Ref. [220]. Copyright (2009) Elsevier.*

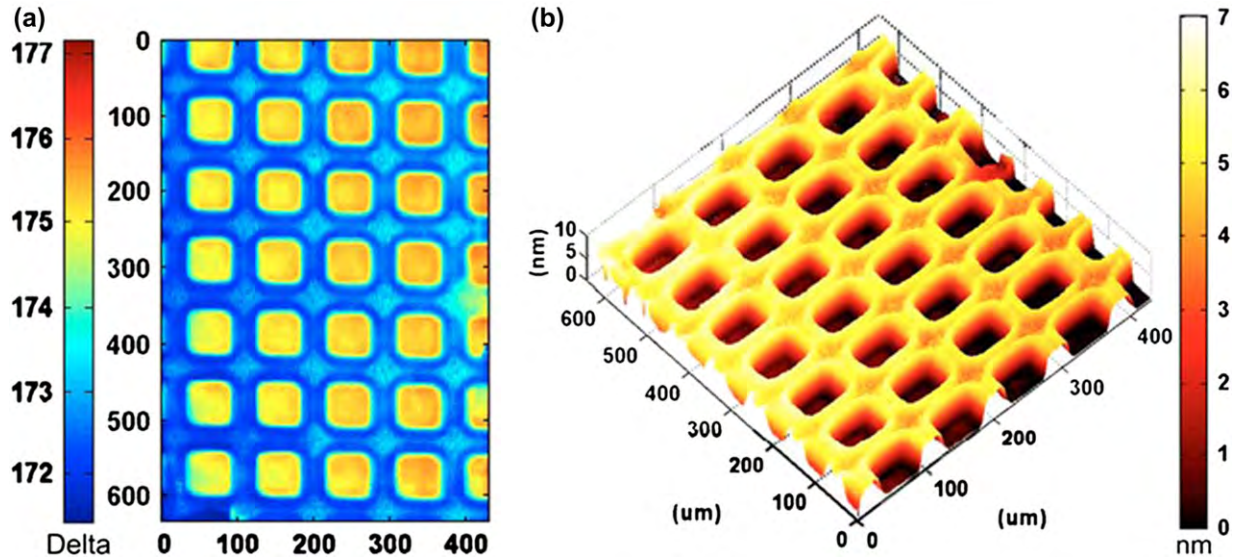

FIGURE 4.38 Ellipsometric characterization of thickness, uniformity, and patterns of supported DMPC membranes. (a) Spatially resolved map of ellipsometric phase shift, Δ, for a micropatterned DMPC bilayer on SiO_2/Si substrate and (b) corresponding thickness map derived using a refractive index of 1.44. *Reprinted with permission from Ref. [224]. Copyright (2007) Elsevier.*

DNA/RHB films decreases exponentially over a period of 12 h when the control DNA/poly(ethylenimine) (DNA/PEI) films show only about 10 nm decrease in the thickness throughout the same period of time.

Ellipsometry can even be extended to imaging ellipsometry by using a monochromatic laser as light source and a CCD camera as the detector. Good contrast among images can be achieved [221–224]. Sapuri-Butti et al. [222] used imaging ellipsometry to characterize the spatially patterned phospholipid bilayers on PDMS substrates with their thickness images. Howland et al. [224] fabricated a micropatterned 1,2-dimyristoyl-*sn*-glycero-3-phosphocholine (DMPC) bilayer on a silicon substrate and then characterized the surface coverage by imaging ellipsometry. As shown in Fig. 4.38, both the phase shift (Δ) and thickness maps indicate the checked pattern of DMPC bilayer.

4.15. CONCLUSIONS

The surface properties can impact critically the success or failure of biomaterials. Consequently, the appropriate surface analytical techniques are crucial to the revelation of important surface properties such as chemistry, topography, hydrophilicity/hydrophobicity, and so on. Generally, a combination of surface characterization methods is recommended to address a problem from different perspectives and to provide more comprehensive information about the biomaterials surface. By taking advantage of these techniques, the *in vitro* and *in vivo* performances of biomaterials can be assessed reliably. In this chapter, we only describe the common surface analytical techniques due to the length limitation and readers are urged to check other references. For instance, colorimetric methods can be utilized to determine the functional groups and immobilized proteins on biomaterials by using specific reagents (coomassie brilliant blue [225], ninhydrin [226], etc.) or kits (bicinchoninic acid kit [227], etc.). Conventional bulk analytical techniques such as X-ray diffraction can also be adopted to determine the crystal structure of biomaterials surface by resorting to a grazing configuration.

REFERENCES

[1] Berkowitz J. Photoabsorption, photoionization, and photoelectron spectroscopy. Academic Press; 1979.

[2] Feldman LC, Mayer JW. Fundamentals of surface and thin film analysis. North Holland-Elsevier; 1986.

[3] He W, Ma ZW, Yong T, Teo WE, Ramakrishna S. Fabrication of collagen-coated biodegradable polymer nanofiber mesh and its potential for endothelial cells growth. Biomaterials 2005;26:7606–15.

[4] Liu XH, Won YJ, Ma PX. Porogen-induced surface modification of nano-fibrous poly (L-lactic acid) scaffolds for tissue engineering. Biomaterials 2006;27:3980–7.

[5] Shen H, Hu XX, Yang F, Bei JZ, Wang SG. Combining oxygen plasma treatment with anchorage of cationized gelatin for enhancing cell affinity of poly(lactide-co-glycolide). Biomaterials 2007;28:4219–30.
[6] Citeau A, Guicheux J, Vinatier C, Layrolle P, Nguyen TP, Pilet P, et al. In vitro biological effects of titanium rough surface obtained by calcium phosphate grid blasting. Biomaterials 2005;26:157–65.
[7] Swan EEL, Popat KC, Desai TA. Peptide-immobilized nanoporous alumina membranes for enhanced osteoblast adhesion. Biomaterials 2005;26:1969–76.
[8] Zhang F, Zhang ZB, Zhu XL, Kang ET, Neoh KG. Silk-functionalized titanium surfaces for enhancing osteoblast functions and reducing bacterial adhesion. Biomaterials 2008;29:4751–9.
[9] Steinmueller-Nethl D, Kloss FR, Najam-U-Haq M, Rainer M, Larsson K, Linsmeier C, et al. Strong binding of bioactive BMP-2 to nanocrystalline diamond by physisorption. Biomaterials 2006;27:4547–56.
[10] Wang HY, Ji JH, Zhang W, Wang W, Zhang YH, Wu ZW, et al. Rat calvaria osteoblast behavior and antibacterial properties of O_2 and N_2 plasma-implanted biodegradable poly(butylene succinate). Acta Biomater 2010;6:154–9.
[11] Wagner CD, Riggs WM, Davis LE, Moulder JF, Muilenberg GE. Handbook of x-ray photoelectron spectroscopy: a reference book of standard data for use in x-ray photoelectron spectroscopy. Perkin-Elmer Corporation; 1979.
[12] Moulder JF, Stickle WF, Sobol PE, Bomben KD. Handbook of x-ray photoelectron spectroscopy: a reference Book of standard spectra for identification and interpretation of XPS data. Perkin-Elmer Corporation; 1992.
[13] Lee KS, Won MS, Noh HB, Shim YB. Triggering the redox reaction of cytochrome c on a biomimetic layer and elimination of interferences for NADH detection. Biomaterials 2010;31:7827–35.
[14] Briggs D, Seah MP. Practical surface analysis by auger and x-ray photoelectron spectroscopy. John Wiley & Sons, Ltd; 1983.
[15] Briggs D, Seah MP. Practical surface analysis (second editon): volume 1- auger and x-ray photoelectron spectroscopy. John Wiley & Sons, Ltd; 1990.
[16] Briggs D, Grant JT. Surface analysis by Auger and x-ray photoelectron spectroscopy. SurfaceSpectra and IM Publications; 2003.
[17] Andrade JD. Surface and interfacial aspects of biomedical polymers: volume 1- surface chemistry and physics. Plenum Press; 1985.
[18] Beamson G, Briggs D. High resolution XPS of organic polymers: the Scienta ESCA300 Database. John Wiley & Sons, Ltd; 1992.
[19] Cao HL, Liu XY, Meng FH, Chu PK. Biological actions of silver nanoparticles embedded in titanium controlled by micro-galvanic effects. Biomaterials 2011;32:693–705.
[20] Arnould C, Volcke C, Lamarque C, Thiry PA, Delhalle J, Mekhalif Z. Titanium modified with layer-by-layer sol-gel tantalum oxide and an organodiphosphonic acid: a coating for hydroxyapatite growth. J Colloid Interface Sci 2009;336:497–503.
[21] Pisarek M, Lewandowska M, Roguska A, Kurzydlowski KJ, Janik-Czachor M. SEM, scanning Auger and XPS characterization of chemically pretreated Ti surfaces intended for biomedical applications. Mater Chem Phys 2007;104:93–7.
[22] Linderback P, Harmankaya N, Askendal A, Areva S, Lausmaa J, Tengvall P. The effect of heat- or ultra violet ozone-treatment of titanium on complement deposition from human blood plasma. Biomaterials 2010;31:4795–801.

[23] Barrere F, van Blitterswijk CA, de Groot K, Layrolle P. Nucleation of biomimetic Ca-P coatings on Ti6Al4V from a SBF X 5 solution: influence of magnesium. Biomaterials 2002;23:2211–20.

[24] Wong MH, Cheng FT, Man HC. Characteristics, apatite-forming ability and corrosion resistance of NiTi surface modified by AC anodization. App Surf Sci 2007;253:7527–34.

[25] Sanada N, Yamamoto A, Oiwa R, Ohashi Y. Extremely low sputtering degradation of polytetrafluoroethylene by C_{60} ion beam applied in XPS analysis. Surf Interface Anal 2004;36:280–2.

[26] Chen YY, Yu BY, Wang WB, Hsu MF, Lin WC, Lin YC, et al. X-ray photoelectron spectrometry depth profiling of organic thin films using C_{60} sputtering. Anal Chem 2008;80:501–5.

[27] Yu BY, Chen YY, Wang WB, Hsu MF, Tsai SP, Lin WC, et al. Depth profiling of organic films with X-ray photoelectron spectroscopy using C_{60}^{+} and Ar^{+} co-sputtering. Anal Chem 2008;80:3412–5.

[28] Rafati A, Davies MC, Shard AG, Hutton S, Mishra G, Alexander MR. Quantitative XPS depth profiling of codeine loaded poly(L-lactic acid) films using a coronene ion sputter source. J Control Release 2009;138:40–4.

[29] Kingshott P, Andersson G, McArthur SL, Griesser HJ. Surface modification and chemical surface analysis of biomaterials. Curr Opin Chem Biol 2011;15:667–76.

[30] Artyushkova K, Farrar JO, Fulghum JE. Data fusion of XPS and AFM images for chemical phase identification in polymer blends. Surf Interface Anal 2009;41:119–26.

[31] Hajati S, Tougaard S, Walton J, Fairley N. Noise reduction procedures applied to XPS imaging of depth distribution of atoms on the nanoscale. Surf Sci 2008;602:3064–70.

[32] Hajati S, Coultas S, Blornfield C, Tougaard S. Nondestructive quantitative XPS imaging of depth distribution of atoms on the nanoscale. Surf Interface Anal 2008;40:688–91.

[33] Vohrer U, Blomfield C, Page S, Roberts A. Quantitative XPS imaging-new possibilities with the delay-line detector. Appl Surf Sci 2005;252:61–5.

[34] Lee CY, Harbers GM, Grainger DW, Gamble LJ, Castner DG. Fluorescence, XPS, and TOF-SIMS surface chemical state image analysis of DNA microarrays. J Am Chem Soc 2007;129:9429–38.

[35] Hedberg CL. Handbook of Auger electron spectroscopy: a book of reference data for identification and interpretation in Auger electron spectroscopy. Physical Electronics, Inc; 1995.

[36] Hanzi AC, Gunde P, Schinhammer M, Uggowitzer PJ. On the biodegradation performance of an Mg-Y-RE alloy with various surface conditions in simulated body fluid. Acta Biomater 2009;5:162–71.

[37] Shabalovskaya SA, Tian H, Anderegg JW, Schryvers DU, Carroll WU, Van Humbeeck J. The influence of surface oxides on the distribution and release of nickel from Nitinol wires. Biomaterials 2009;30:468–77.

[38] Xue WC, Liu XY, Zheng XB, Ding CX. In vivo evaluation of plasma-sprayed titanium coating after alkali modification. Biomaterials 2005;26:3029–37.

[39] Nakai M, Niinomi M, Akahori T, Ohtsu N, Nishimura H, Toda H, et al. Surface hardening of biomedical Ti-29Nb-13Ta-4.6Zr and Ti-6Al-4V ELI by gas nitriding. Mater Sci Eng A 2008;486:193–201.

[40] Jiang XR, Chen R, Bent SF. Spatial control over atomic layer deposition using micro-contact-printed resists. Surf Coat Technol 2007;201:8799–807.

[41] Wang ZX, Liu JY, Zhang K, Cai HB, Zhang GH, Wu YK, et al. Fabrication of well-aligned and highly dense cadmium sulfide nanowires on DNA scaffolds using the poly (dimethylsiloxane) transfer method. J Phys Chem C 2009;113:5428–33.
[42] Watanabe S, Shibata H, Sakamoto F, Azumi R, Sakai H, Abe M, et al. Directed self-assembly of gold nanoparticles and gold thin films on micro- and nanopatterned templates fabricated from mixed phase-separated Langmuir-Blodgett films. J Mater Chem 2009;19:6796–803.
[43] Vickerman JC, Brown A, Reed NM. Secondary ion mass spectrometry, principles and applications. Oxford University Press; 1989.
[44] Behrisch R. Sputtering by particle bombardment I: physical sputtering of single-element solids. Springer-Verlag; 1981.
[45] Behrisch R. Sputtering by particle bombardment II: sputtering of alloys and compounds, electron and neuron sputtering, surface topography. Springer-Verlag; 1983.
[46] Behrisch R, Wittmaack K. Sputtering by particle bombardment III: characteristics of sputtered particles, technical applications. Springer-Verlag; 1991.
[47] Behrisch R, Eckstein W. Sputtering by particle bombardment: experiments and computer calculations from threshold to MeV energies. Springer-Verlag; 2007.
[48] Benninghoven A, Rüdenauer FG, Werner HW. Secondary ion mass spectrometry: basic concepts, instrumental aspects, applications, and trends. John Wiley & Sons, Ltd; 1987.
[49] Vickerman JC, Briggs D. ToF-SIMS: surface analysis by mass spectrometry. SurfaceSpectra and IM Publications; 2001.
[50] Tidwell CD, Castner DG, Golledge SL, Ratner BD, Meyer K, Hagenhoff B, et al. Static time-of-light secondary ion mass spectrometry and X-ray photoelectron spectroscopy characterization of adsorbed albumin and fibronectin films. Surf Interface Anal 2001;31:724–33.
[51] von Vacano B, Xu R, Hirth S, Herzenstiel I, Ruckel M, Subkowski T, et al. Hydrophobin can prevent secondary protein adsorption on hydrophobic substrates without exchange. Anal Bioanal Chem 2011;400:2031–40.
[52] Killian MS, Krebs HM, Schmuki P. Protein denaturation detected by time-of-flight secondary ion mass spectrometry. Langmuir 2011;27:7510–5.
[53] Salerno S, Piscioneri A, Laera S, Morelli S, Favia P, Bader A, et al. Improved functions of human hepatocytes on NH_3 plasma-grafted PEEK-WC–PU membranes. Biomaterials 2009;30:4348–56.
[54] Pidhatika B, Moller J, Benetti EM, Konradi R, Rakhmatullina E, Muhlebach A, et al. The role of the interplay between polymer architecture and bacterial surface properties on the microbial adhesion to polyoxazoline-based ultrathin films. Biomaterials 2010;31:9462–72.
[55] Vickerman JC, Gilmore IS. Surface analysis-the principal techniques. John Wiley & Sons, Ltd; 2009.
[56] Barnes CA, Brison J, Michel R, Brown BN, Castner DG, Badylak SF, et al. The surface molecular functionality of decellularized extracellular matrices. Biomaterials 2011;32:137–43.
[57] Brown BN, Barnes CA, Kasick RT, Michel R, Gilbert TW, Beer-Stolz D, et al. Surface characterization of extracellular matrix scaffolds. Biomaterials 2010;31:428–37.
[58] Yang J, Mei Y, Hook AL, Taylor M, Urquhart AJ, Bogatyrev SR, et al. Polymer surface functionalities that control human embryoid body cell adhesion revealed by high throughput surface characterization of combinatorial material microarrays. Biomaterials 2010;31:8827–38.

[59] Tyler BJ, Bruening C, Rangaranjan S, Arlinghaus HF. TOF-SIMS imaging of adsorbed proteins on topographically complex surfaces with Bi^{3+} primary ions. Biointerphases 2011;6:135–41.

[60] Vaezian B, Anderton CR, Kraft ML. Discriminating and imaging different phosphatidylcholine species within phase-separated model membranes by principal component analysis of TOF-secondary ion mass spectrometry images. Anal Chem 2010;82:10002–14.

[61] Liu F, Dubey M, Takahashi H, Castner DG, Grainger DW. Immobilized antibody orientation analysis using secondary ion mass spectrometry and fluorescence imaging of affinity-generated patterns. Anal Chem 2010;82:2947–58.

[62] Dubey M, Emoto K, Takahashi H, Castner DG, Grainger DW. Affinity-based protein surface pattern formation by ligand self-selection from mixed protein solutions. Adv Funct Mater 2009;19:3046–55.

[63] Ogaki R, Lyckegaard F, Kingshott P. High resolution surface chemical analysis of a trifunctional pattern made by sequential colloidal shadowing. Chem Phys Chem 2010;11:3609–16.

[64] Ogaki R, Cole MA, Sutherland DS, Kingshott P. Microcup arrays featuring multiple chemical regions patterned with nanoscale precision. Adv Mater 2011;23:1876–81.

[65] Tyler BJ, Rayal G, Castner DG. Multivariate analysis strategies for processing ToF-SIMS images of biomaterials. Biomaterials 2007;28:2412–23.

[66] Park JW, Min H, Kim YP, Shon HK, Kim J, Moon DW, et al. Multivariate analysis of ToF-SIMS data for biological applications. Surf Interface Anal 2009;41:694–703.

[67] Lamolle SF, Monjo M, Rubert M, Haugen HJ, Lyngstadaas SP, Ellingsen JE. The effect of hydrofluoric acid treatment of titanium surface on nanostructural and chemical changes and the growth of MC3T3-E1 cells. Biomaterials 2009;30:736–42.

[68] Lechene C, Hillion F, McMahon G, Benson D, Kleinfeld AM, Kampf JP, et al. High-resolution quantitative imaging of mammalian and bacterial cells using stable isotope mass spectrometry. J Biol 2006;5:20.

[69] Tyler BJ, Takeno MM, Hauch KD. Identification and Imaging of ^{15}N labeled cells with ToF-SIMS. Surf Interface Anal 2011;43:336–9.

[70] Cheng J, Wucher A, Winograd N. Molecular depth profiling with cluster ion beams. J Phys Chem B 2006;110:8329–36.

[71] Cheng J, Winograd N. Depth profiling of peptide films with TOF-SIMS and a C_{60} Probe. Anal Chem 2005;77:3651–9.

[72] Shard AG, Green FM, Brewer PJ, Seah MP, Gilmore IS. Quantitative molecular depth profiling of organic delta-layers by C_{60} ion sputtering and SIMS. J Phys Chem B 2008;112:2596–605.

[73] Fletcher JS, Lockyer NP, Vaidyanathan S, Vickerman JC. TOF-SIMS 3D biomolecular imaging of xenopus laevis oocytes using buckminsterfullerene (C_{60}) primary ions. Anal Chem 2007;79:2199–206.

[74] Wucher A, Cheng J, Winograd N. Protocols for three-dimensional molecular imaging using mass spectrometry. Anal Chem 2007;79:5529–39.

[75] Clarke B, Kingshott P, Hou X, Rochev Y, Gorelov A, Carroll W. Effect of nitinol wire surface properties on albumin adsorption. Acta Biomater 2007;3:103–11.

[76] Heuts J, Salber J, Goldyn AM, Janser R, Moller M, Klee D. Bio-functionalized star PEG-coated PVDF surfaces for cytocompatibility-improved implant components. J Biomed Mater Res A 2009;92A:1538–51.

[77] Boyd AR, Burke GA, Duffy H, Holmberg M, Kane CO, Meenan BJ, et al. Sputter deposited bioceramic coatings: surface characterization and initial protein adsorption studies using surface-MALDI-MS. J Mater Sci mater Med 2011;22:71–84.
[78] Groll J, Ademovic Z, Ameringer T, Klee D, Moeller M. Comparison of coatings from reactive star shaped PEG-stat-PPG prepolymers and grafted linear PEG for biological and medical applications. Biomacromolecules 2005;6:956–62.
[79] Ademovic Z, Gonera A, Mischnick P, Klee D. Biocompatible surface preparation using amino-functionalized amylase. Biomacromolecules 2006;7:1429–32.
[80] Griesser HJ, Kingshott P, McArthur SL, McLean KM, Kinsel GR, Timmons RB. Surface-MALDI mass spectrometry in biomaterials research. Biomaterials 2004;25:4861–75.
[81] Ma DHK, Lai JY, Cheng HY, Tsai CC, Yeh LK. Carbodiimide cross-linked amniotic membranes for cultivation of limbal epithelial cells. Biomaterials 2010;31:6647–58.
[82] Blaker JJ, Bismarck A, Boccaccini AR, Young AM, Nazhat SN. Premature degradation of poly(α-hydroxyesters) during thermal processing of Bioglass®-containing composites. Acta Biomater 2010;6:756–62.
[83] Rebollar E, Frischauf I, Olbrich M, Peterbauer T, Hering S, Preiner J, et al. Proliferation of aligned mammalian cells on laser-nanostructured polystyrene. Biomaterials 2008;29:1796–806.
[84] Simons WW. The Sadtler handbook of infrared spectra. Sadtler Research Laboratories; 1978.
[85] Chalmers JM, Griffiths PR. Handbook of vibrational spectroscopy. John Wiley & Sons, Ltd; 2002.
[86] Greenler RG. Infrared study of adsorbed molecules on metal surfaces by reflection techniques. J Chem Phys 1966;44:310–5.
[87] Freitas SC, Barbosa MA, Martins MCL. The effect of immobilization of thrombin inhibitors onto self-assembled monolayers on the adsorption and activity of thrombin. Biomaterials 2010;31:3772–80.
[88] Humblot V, Yala JF, Thebault P, Boukerma K, Hequet A, Berjeaud JM, et al. The antibacterial activity of Magainin I immobilized onto mixed thiols self-assembled monolayers. Biomaterials 2009;30:3503–12.
[89] Briand E, Salmain M, Compere C, Pradier CM. Anti-rabbit immunoglobulin G detection in complex medium by PM-RAIRS and QCM influence of the antibody immobilisation method. Biosens Bioelectron 2007;22:2884–90.
[90] Harding DJ, Gruene P, Haertelt M, Meijer G, Fielicke A, Hamilton SM, et al. Probing the structures of gas-phase rhodium cluster cations by far-infrared spectroscopy. J Chem Phys 2010;133:214304.
[91] Prati S, Sciutto G, Mazzeo R, Torri C, Fabbri D. Application of ATR-far-infrared spectroscopy to the analysis of natural resins. Anal Bioanal Chem 2011;399:3081–91.
[92] Meyer T, Bergner N, Bielecki C, Krafft C, Akimov D, Romeike BFM, et al. Nonlinear microscopy, infrared, and Raman microspectroscopy for brain tumor analysis. J Biomed Opt 2011;16:021113.
[93] Lee ES, Lee JY. High resolution cellular imaging with nonlinear optical infrared microscopy. Opt Express 2011;19:1378–84.
[94] Schrader B. Infrared and Raman spectroscopy: methods and applications. Wiley-VCH; 1995.
[95] Lewis IR, Edwards HGM. Handbook of Raman spectroscopy: from the research laboratory to the process line. Marcel Dekker, Inc; 2001.

[96] Wang HY, Xu M, Zhang W, Kwok DTK, Jiang J, Wu ZW, et al. Mechanical and biological characteristics of diamond-Like carbon coated poly aryl-ether-ether-ketone. Biomaterials 2010;31:8181–7.
[97] Saber-Samandari S, Gross KA. The use of thermal printing to control the properties of calcium phosphate deposits. Biomaterials 2010;31:6386–93.
[98] Ku SH, Park CB. Human endothelial cell growth on mussel-inspired nanofiber scaffold for vascular tissue engineering. Biomaterials 2010;31:9431–7.
[99] Lopez-Heredia MA, Sohier J, Gaillard C, Quillard S, Dorget M, Layrolle P. Rapid prototyped porous titanium coated with calcium phosphate as a scaffold for bone tissue engineering. Biomaterials 2008;29:2608–15.
[100] Fang JX, Liu SY, Li ZY. Polyhedral silver mesocages for single particle surface-enhanced Raman scattering-based biosensor. Biomaterials 2011;32:4877–84.
[101] Qian J, Jiang L, Cai FH, Wang D, He SL. Fluorescence-surface enhanced Raman scattering co-functionalized gold nanorods as near-infrared probes for purely optical in vivo imaging. Biomaterials 2011;32:1601–10.
[102] Noh MS, Jun BH, Kim S, Kang H, Woo MA, Minai-Tehrani A, et al. Magnetic surface-enhanced Raman spectroscopic (M-SERS) dots for the identification of bronchioalveolar stem cells in normal and lung cancer mice. Biomaterials 2009;30:3915–25.
[103] Liu XW, Tao HQ, Yang K, Zhang SA, Lee ST, Liu ZA. Optimization of surface chemistry on single-walled carbon nanotubes for in vivo photothermal ablation of tumors. Biomaterials 2011;32:144–51.
[104] Egerton RF, Cheng SC. Measurement of local thickness by electron energy-loss spectroscopy. Ultramicroscopy 1987;21:231–44.
[105] Malis T, Cheng SC, Egerton RF. EELS log-ratio technique for specimen-thickness measurement in the TEM. J Electron Microsc Tech 1988;8:193–200.
[106] Egerton RF. Electron energy-loss spectroscopy in the electron microscope. Plenum; 1996.
[107] Ma WJ, Ruys AJ, Mason RS, Martin PJ, Bendavid A, Liu ZW, et al. DLC coatings: effects of physical and chemical properties on biological response. Biomaterials 2007;28:1620–8.
[108] Gries K, Kroger R, Kubel C, Fritz M, Rosenauer A. Investigations of voids in the aragonite platelets of nacre. Acta Biomater 2009;5:3038–44.
[109] Heimann RB, Wirth R. Formation and transformation of amorphous calcium phosphates on titanium alloy surfaces during atmospheric plasma spraying and their subsequent in vitro performance. Biomaterials 2006;27:823–31.
[110] Liou SC, Chen SY, Lee HY, Bow JS. Structural characterization of nano-sized calcium deficient apatite powders. Biomaterials 2004;25:189–96.
[111] Zhou YY, Shi LX, Li QN, Jiang H, Lv G, Zhao J, et al. Imaging and inhibition of multi-drug resistance in cancer cells via specific association with negatively charged CdTe quantum dots. Biomaterials 2010;31:4958–63.
[112] Matsusaki M, Yoshida H, Akashi M. The construction of 3D-engineered tissues composed of cells and extracellular matrices by hydrogel template approach. Biomaterials 2007;28:2729–37.
[113] Murphy AR, John PS, Kaplan DL. Modification of silk fibroin using diazonium coupling chemistry and the effects on hMSC proliferation and differentiation. Biomaterials 2008;29:2829–38.
[114] Ding YJ, Liu J, Wang H, Shen GL, Yu RQ. A piezoelectric immunosensor for the detection of α-fetoprotein using an interface of gold/hydroxyapatite hybrid nanomaterial. Biomaterials 2007;28:2147–54.

[115] Lin JJ, Chen JS, Huang SJ, Ko JH, Wang YM, Chen TL, et al. Folic acid-Pluronic F127 magnetic nanoparticle clusters for combined targeting, diagnosis, and therapy applications. Biomaterials 2009;30:5114–24.

[116] Tong J, Zimmerman MC, Li SM, Yi X, Luxenhofer R, Jordan R, et al. Neuronal uptake and intracellular superoxide scavenging of a fullerene (C60)-poly(2-oxazoline)s nanoformulation. Biomaterials 2011;32:3654–65.

[117] Mao ZW, Ma L, Yan J, Yan M, Gao CY, Shen JC. The gene transfection efficiency of thermoresponsive N, N, N-trimethyl chitosan chloride-g-poly(N-isopropylacrylamide) copolymer. Biomaterials 2007;28:4488–500.

[118] Van den Beucken JJJP, Vos MRJ, Thune PC, Hayakawa T, Fukushima T, Okahata Y, et al. Fabrication, characterization, and biological assessment of multilayered DNA-coatings for biomaterial purposes. Biomaterials 2006;27:691–701.

[119] Yang MH, Yang Y, Yang HF, Shen GL, Yu RQ. Layer-by-layer self-assembled multilayer films of carbon nanotubes and platinum nanoparticles with polyelectrolyte for the fabrication of biosensors. Biomaterials 2006;27:246–55.

[120] Lee T, Min J, Kim SU, Choi JW. Multifunctional 4-bit biomemory chip consisting of recombinant azurin variants. Biomaterials 2011;32:3815–21.

[121] Ji Y, Ghosh K, Shu XZ, Li BQ, Sokolov JC, Prestwich GD, et al. Electrospun three-dimensional hyaluronic acid nanofibrous scaffolds. Biomaterials 2006;27:3782–92.

[122] Tai BCU, Wan ACA, Ying JY. Modified polyelectrolyte complex fibrous scaffold as a matrix for 3D cell culture. Biomaterials 2010;31:5927–35.

[123] Pang YG, Ucuzian AA, Matsumura A, Brey EM, Gassman AA, Husak VA. The temporal and spatial dynamics of microscale collagen scaffold remodeling by smooth muscle cells. Biomaterials 2009;30:2023–31.

[124] Thibault M, Astolfi M, Tran-Khanh N, Lavertu M, Darras V, Merzouki A, et al. Excess polycation mediates efficient chitosan-based gene transfer by promoting lysosomal release of the polyplexes. Biomaterials 2011;32:4639–46.

[125] Kim SJ, Ise H, Goto M, Komura K, Cho CS, Akaike T. Gene delivery system based on highly specific recognition of surface-vimentin with N-acetylglucosamine immobilized polyethylenimine. Biomaterials 2011;32:3471–80.

[126] Cross VL, Zheng Y, Choi NW, Verbridge SS, Sutermaster BA, Bonassar LJ, et al. Dense type I collagen matrices that support cellular remodeling and microfabrication for studies of tumor angiogenesis and vasculogenesis in vitro. Biomaterials 2010;31:8596–607.

[127] Blakeney BA, Tambralli A, Anderson JM, Andukuri A, Lim DJ, Dean DR, et al. Cell infiltration and growth in a low density, uncompressed three-dimensional electrospun nanofibrous scaffold. Biomaterials 2011;32:1583–90.

[128] Da Silva J, Lautenschlager F, Sivaniah E, Guck JR. The cavity-to-cavity migration of leukaemic cells through 3D honey-combed hydrogels with adjustable internal dimension and stiffness. Biomaterials 2010;31:2201–8.

[129] Pang YG, Wang XL, Ucuzian AA, Brey EM, Burgess WH, Jones KJ, et al. Local delivery of a collagen-binding FGF-1 chimera to smooth muscle cells in collagen scaffolds for vascular tissue engineering. Biomaterials 2010;31:878–85.

[130] Futaba DN, Hata K, Namai T, Yamada T, Mizuno K, Hayamizu Y, et al. 84% catalyst activity of water-assisted growth of single walled carbon nanotube forest characterization by a statistical and macroscopic approach. J Phys Chem B 2006;110:8035–8.

[131] Park J, Bauer S, von der Mark K, Schmuki P. Nanosize and vitality: TiO_2 nanotube diameter directs cell fate. Nano Letters 2007;7:1686–91.

[132] Oh S, Brammer KS, Li YSJ, Teng D, Engler AJ, Chien S, et al. Stem cell fate dictated solely by altered nanotube dimension. Proc Natl Acad Sci U S A 2009;106:2130–5.
[133] Rujitanaroj PO, Wang YC, Wang J, Chew SY. Nanofiber-mediated controlled release of siRNA complexes for long term gene-silencing applications. Biomaterials 2011;32:5915–23.
[134] He CL, Xiao GY, Jin XB, Sun CH, Ma PX. Electrodeposition on nanofibrous polymer scaffolds: rapid mineralization, tunable calcium phosphate composition and topography. Adv Funct Mater 2010;20:3568–76.
[135] Yuk SH, Oh KS, Koo H, Jeon H, Kim K, Kwon IC. Multi-core vesicle nanoparticles based on vesicle fusion for delivery of chemotherapic drugs. Biomaterials 2011;32:7924–31.
[136] Kai D, Prabhakaran MP, Jin GR, Ramakrishna S. Guided orientation of cardiomyocytes on electrospun aligned nanofibers for cardiac tissue engineering. J Biomed Mater Res B 2011;98B:379–86.
[137] Lamers E, Walboomers XF, Domanski M, te Riet J, van Delft FCMJM, Luttge R, et al. The influence of nanoscale grooved substrates on osteoblast behavior and extracellular matrix deposition. Biomaterials 2010;31:3307–16.
[138] Wang HY, Ji JH, Zhang W, Zhang YH, Jiang J, Wu ZW, et al. Biocompatibility and bioactivity of plasma-treated biodegradable poly(butylene succinate). Acta Biomater 2009;5:279–87.
[139] Antunes JC, Oliveira JM, Reis RL, Soria JM, Gomez-Ribelles JL, Mano JF. Novel poly(L-lactic acid)/hyaluronic acid macroporous hybrid scaffolds: characterization and assessment of cytotoxicity. J Biomed Mater Res A 2010;94A:856–69.
[140] Zhang KH, Qian YF, Wang HS, Fan LP, Huang C, Yin AL, et al. Genipin-crosslinked silk fibroin/hydroxybutyl chitosan nanofibrous scaffolds for tissue-engineering application. J Biomed Mater Res A 2010;95A:870–81.
[141] Reis ECC, Borges APB, Araujo MVF, Mendes VC, Guan LM, Davies JE. Periodontal regeneration using a bilayered PLGA/calcium phosphate construct. Biomaterials 2011;32:9244–53.
[142] Daculsi G, Goyenvalle E, Cognet R, Aguado E, Suokas EO. Osteoconductive properties of poly(96L/4D-lactide)/beta-tricalcium phosphate in long term animal model. Biomaterials 2011;32:3166–77.
[143] Bandyopadhyay-Ghosh S, Faria PEP, Johnson A, Felipucci DNB, Reaney IM, Salata LA, et al. Osteoconductivity of modified fluorcanasite glass–ceramics for bone tissue augmentation and repair. J Biomed Mater Res A 2010;94A:760–8.
[144] Kusakabe H, Sakamaki T, Nihei K, Oyama Y, Yanagimoto S, Ichimiya M, et al. Osseointegration of a hydroxyapatite-coated multilayered mesh stem. Biomaterials 2004;25:2957–69.
[145] Zinelis S, Barmpagadaki X, Vergos V, Chakmakchi M, Eliades G. Bond strength and interfacial characterization of eight low fusing porcelains to cp Ti. Dent Mater 2010;26:264–73.
[146] Zhang Y, Yin QS, Zhang Y, Xia H, Ai FZ, Jiao YP, et al. Determination of antibacterial properties and cytocompatibility of silver-loaded coral hydroxyapatite. J Mater Sci Mater Med 2010;21:2453–62.
[147] Variola F, Yi JH, Richert L, Wuest JD, Rosei F, Nanci A. Tailoring the surface properties of Ti6Al4V by controlled chemical oxidation. Biomaterials 2008;29:1285–98.
[148] Han B, Wang XY, Gao XJ, Liu JG, Liang FX, Qu XZ, et al. Synthesis and characterization of biodegradable microcapsules for the controlled delivery of calcium hydroxide. J Biomed Mater Res B 2011;99B:120–6.

[149] Coelho PG, Lemons JE. Physico/chemical characterization and in vivo evaluation of nanothickness bioceramic depositions on alumina-blasted/acid-etched Ti-6Al-4V implant surfaces. J Biomed Mater Res A 2009;90A:351–61.
[150] Khaled SMZ, Charpentier PA, Rizkalla AS. Synthesis and characterization of poly(methyl methacrylate)-based experimental bone cements reinforced with TiO_2-SrO nanotubes. Acta Biomater 2010;6:3178–86.
[151] Danilatos GD. Environmental scanning electron microscopy. In: In-situ microscopy in materials research: leading international research in electron and scanning probe microscopies. Kluwer Academic Publishers; 1997.
[152] Fundueanu G, Constantin M, Oanea I, Harabagiu V, Ascenzi P, Simionescu BC. Entrapment and release of drugs by a strict "on-off" mechanism in pullulan microspheres with pendant thermosensitive groups. Biomaterials 2010;31:9544–53.
[153] Fang Y, Yu H, Chen L, Chen S. Facile glycerol-assisted synthesis of N-vinyl pyrrolidinone-based thermosensitive hydrogels via frontal polymerization. Chem Mater 2009;21:4711–8.
[154] Tian HY, Deng C, Lin H, Sun JR, Deng MX, Chen XS, et al. Biodegradable cationic PEG–PEI–PBLG hyperbranched block copolymer: synthesis and micelle characterization. Biomaterials 2005;26:4209–17.
[155] Ma PA, Liu S, Huang YB, Chen XS, Zhang LP, Jing XB. Lactose mediated liver-targeting effect observed by ex vivo imaging technology. Biomaterials 2010;31:2646–54.
[156] Shi Q, Chen XS, Lu TC, Jing XB. The immobilization of proteins on biodegradable polymer fibers via click chemistry. Biomaterials 2008;29:1118–26.
[157] Taylor JE, Laity PR, Hicks J, Wong SS, Norris K, Khunkamchoo P, et al. Extent of iron pick-up in deforoxamine-coupled polyurethane materials for therapy of chronic wounds. Biomaterials 2005;26:6024–33.
[158] Lusvardi G, Zaffe D, Menabue L, Bertoldi C, Malavasi G, Consolo U. In vitro and in vivo behaviour of zinc-doped phosphosilicate glasses. Acta Biomater 2009;5:419–28.
[159] Zareie HM, Boyer C, Bulmus V, Nateghi E, Davis TP. Temperature-responsive self-assembled monolayers of oligo(ethylene glycol): control of biomolecular recognition. ACS Nano 2008;2:757–65.
[160] Kim SU, Yagati AK, Min JH, Choi JW. Nanoscale protein-based memory device composed of recombinant azurin. Biomaterials 2010;31:1293–8.
[161] Yang NJ, Uetsuka H, Williams OA, Osawa E, Tokuda N, Nebel CE. Vertically aligned diamond nanowires: fabrication, characterization, and application for DNA sensing. Physica Status Solidi A 2009;206:2048–56.
[162] Odom TW, Huang JL, Kim P, Lieber CM. Atomic structure and electronic properties of single-walled carbon nanotubes. Nature 1998;391:62–4.
[163] Ouyang M, Huang JL, Cheung CL, Lieber CM. Energy gaps in "metallic" single-walled carbon nanotubes. Science 2001;292:702–5.
[164] Ma DDD, Lee CS, Au FCK, Tong SY, Lee ST. Small-diameter silicon nanowire surfaces. Science 2003;299:1874–7.
[165] Coraux J, N'Diaye AT, Busse C, Michely T. Structural coherency of graphene on Ir(111). Nano Lett 2008;8:565–70.
[166] Ishigami M, Chen JH, Cullen WG, Fuhrer MS, Williams ED. Atomic structure of graphene on SiO_2. Nano Lett 2007;7:1643–8.
[167] Binnig G, Quate CF, Gerber C. Atomic force microscope. Phys Rev Lett 1986;56:930–3.

[168] Ebeling D, Holscher H, Fuchs H, Anczykowski B, Schwarz UD. Imaging of biomaterials in liquids: a comparison between conventional and Q-controlled amplitude modulation ('tapping mode') atomic force microscopy. Nanotechnology 2006;17:S221–6.
[169] Zhou M, Smith AM, Das AK, Hodson NW, Collins RF, Ulijn RV, et al. Self-assembled peptide-based hydrogels as scaffolds for anchorage-dependent cells. Biomaterials 2009;30:2523–30.
[170] Ye Z, Zhao X. Phase imaging atomic force microscopy in the characterization of biomaterials. J Microsc 2010;238:27–35.
[171] He LM, Liao SS, Quan DP, Ngiam M, Chan CK, Ramakrishna S, et al. The influence of laminin-derived peptides conjugated to Lys-capped PLLA on neonatal mouse cerebellum C17.2 stem cells. Biomaterials 2009;30:1578–86.
[172] Xu LC, Runt J, Siedlecki CA. Dynamics of hydrated polyurethane biomaterials: surface microphase restructuring, protein activity and platelet adhesion. Acta Biomater 2010;6:1938–47.
[173] Hentschel J, Boerner HG. Peptide-directed microstructure formation of polymers in organic media. J Am Chem Soc 2006;128:14142–9.
[174] Pallandre A, Glinel K, Jonas AM, Nysten B. Binary nanopatterned surfaces prepared from silane monolayers. Nano Lett 2004;4:365–71.
[175] Denis FA, Pallandre A, Nysten B, Jonas AM, Dupont-Gillain CC. Alignment and assembly of adsorbed collagen molecules induced by anisotropic chemical nanopatterns. Small 2005;1:984–91.
[176] Baralia GG, Pallandre A, Nysten B, Jonas AM. Nanopatterned self-assembled monolayers. Nanotechnology 2006;17:1160–5.
[177] Qin GK, Lapidot S, Numata K, Hu X, Meirovitch S, Dekel M, et al. Expression, cross-linking, and characterization of recombinant chitin binding resilin. Biomacromolecules 2009;10:3227–34.
[178] Hu XA, Wang XL, Rnjak J, Weiss AS, Kaplan DL. Biomaterials derived from silk-tropoelastin protein systems. Biomaterials 2010;31:8121–31.
[179] Block S, Glockl G, Weitschies W, Helm CA. Direct visualization and identification of biofunctionalized nanoparticles using a magnetic atomic force microscope. Nano Lett 2011;11:3587–92.
[180] Kienberger F, Ebner A, Gruber HJ, Hinterdorfer P. Molecular recognition imaging and force spectroscopy of single biomolecules. Acc Chem Res 2006;39:29–36.
[181] Sima F, Davidson P, Pauthe E, Sima LE, Gallet O, Mihailescu IN, et al. Fibronectin layers by matrix-assisted pulsed laser evaporation from saline buffer-based cryogenic targets. Acta Biomater 2011;7:3780–8.
[182] Park JW, Jang JH, Lee CS, Hanawa T. Osteoconductivity of hydrophilic microstructured titanium implants with phosphate ion chemistry. Acta Biomater 2009;5:2311–21.
[183] Barranco V, Escudero ML, Garcia-Alonso MC. Influence of the microstructure and topography on the barrier properties of oxide scales generated on blasted Ti6Al4V surfaces. Acta Biomater 2011;7:2716–25.
[184] Park JW, Kim HK, Kim YJ, Jang JH, Song H, Hanawa T. Osteoblast response and osseointegration of a Ti-6Al-4V alloy implant incorporating strontium. Acta Biomater 2010;6:2843–51.
[185] Park JW, Kim YJ, Jang JH, Kwon TG, Bae YC, Suh JY. Effects of phosphoric acid treatment of titanium surfaces on surface properties, osteoblast response and removal of torque forces. Acta Biomater 2010;6:1661–70.

[186] Truong VK, Lapovok R, Estrin YS, Rundell S, Wang JY, Fluke CJ, et al. The influence of nano-scale surface roughness on bacterial adhesion to ultrafine-grained titanium. Biomaterials 2010;31:3674–83.
[187] Park JW, Park KB, Suh JY. Effects of calcium ion incorporation on bone healing of Ti6Al4V alloy implants in rabbit tibiae. Biomaterials 2007;28:3306–13.
[188] Turssi CP, Ferracane JL, Vogel K. Filler features and their effects on wear and degree of conversion of particulate dental resin composites. Biomaterials 2005;26:4932–7.
[189] Huang FL, Wei QF, Wang XQ, Xu WZ. Dynamic contact angles and morphology of PP fibres treated with plasma. Polym Test 2006;25:22–7.
[190] Wortmann FJ, Wortmann G, zur Wiesche ES. Spatial probing of the properties of the human hair surface using Wilhelmy force profiles. Langmuir 2010;26:7365–9.
[191] Yum K, Yu MF. Measurement of wetting properties of individual boron nitride nanotubes with the Wilhelmy method using a nanotube-based force sensor. Nano Lett 2006;6:329–33.
[192] Yazdanpanah MM, Hosseini M, Pabba S, Berry SM, Dobrokhotov VV, Safir A, et al. Micro-Wilhelmy and related liquid property measurements using constant-diameter nanoneedle-tipped atomic force microscope probes. Langmuir 2008;24:13753–64.
[193] Stachewicz U, Barber AH. Enhanced wetting behavior at electrospun polyamide nanofiber surfaces. Langmuir 2011;27:3024–9.
[194] Tadmor R. Line energy and the relation between advancing, receding, and young contact angles. Langmuir 2004;20:7659–64.
[195] Chibowski E, Terpilowski K. Surface free energy of sulfur—revisited I. Yellow and orange samples solidified against glass surface. J Colloid Interface Sci 2008;319:505–13.
[196] Yamanlar S, Sant S, Boudou T, Picart C, Khademhosseini A. Surface functionalization of hyaluronic acid hydrogels by polyelectrolyte multilayer films. Biomaterials 2011;32: 5590–9.
[197] Alauzun JG, Young S, D'Souza R, Liu L, Brook MA, Sheardown HD. Biocompatible, hyaluronic acid modified silicone elastomers. Biomaterials 2010;31:3471–8.
[198] Kyomoto M, Moro T, Takatori Y, Kawaguchi H, Nakamura K, Ishihara K. Self-initiated surface grafting with poly(2-methacryloyloxyethyl phosphorylcholine) on poly(ether-ether-ketone). Biomaterials 2010;31:1017–24.
[199] Alibeik S, Zhu SP, Yau JW, Weitz JI, Brash JL. Surface modification with polyethylene glycol-corn trypsin inhibitor conjugate to inhibit the contact factor pathway on blood-contacting surfaces. Acta Biomater 2011;7:4177–86.
[200] Feng XJ, Jiang L. Design and creation of superwetting/antiwetting surfaces. Adv Mater 2006;18:3063–78.
[201] Ma ZW, Kotaki M, Yong T, He W, Ramakrishna S. Surface engineering of electrospun polyethylene terephthalate (PET) nanofibers towards development of a new material for blood vessel engineering. Biomaterials 2005;26:2527–36.
[202] Ma ZW, He W, Yong T, Ramakrishna S. Grafting of gelatin on electrospun poly(-caprolactone) nanofibers to improve endothelial cell spreading and proliferation and to control cell orientation. Tissue Eng 2005;11:1149–58.
[203] Wang HY, Kwok DTK, Wang W, Wu ZW, Tong LP, Zhang YM, et al. Osteoblast behavior on polytetrafluoroethylene modified by long pulse, high frequency oxygen plasma immersion ion implantation. Biomaterials 2010;31:413–9.
[204] Feng B, Weng J, Yang BC, Qu SX, Zhang XD. Characterization of surface oxide films on titanium and adhesion of osteoblast. Biomaterials 2003;24:4663–70.
[205] Michiardi A, Aparicio C, Ratner BD, Planell JA, Gil J. The influence of surface energy on competitive protein adsorption on oxidized NiTi surfaces. Biomaterials 2007;28:586–94.

[206] Ochsenbein A, Chai F, Winter S, Traisnel M, Breme J, Hildebrand HF. Osteoblast responses to different oxide coatings produced by the sol-gel process on titanium substrates. Acta Biomater 2008;4:1506–17.

[207] Ruttermann S, Trellenkamp T, Bergmann N, Raab WHM, Ritter H, Janda R. A new approach to influence contact angle and surface free energy of resin-based dental restorative materials. Acta Biomater 2011;7:1160–5.

[208] Bernard SA, Balla VK, Davies NM, Bose S, Bandyopadhyay A. Bone cell-materials interactions and Ni ion release of anodized equiatomic NiTi alloy. Acta Biomater 2011;7:1902–12.

[209] Bozukova D, Pagnoulle C, De Pauw-Gillet MC, Desbief S, Lazzaroni R, Ruth N. Improved performances of intraocular lenses by poly(ethylene glycol) chemical coatings. Biomacromolecules 2007;8:2379–87.

[210] Wan LS, Xu ZK, Huang XJ, Wang ZG, Ye P. Hemocompatibility of poly(acrylonitrile-co-N-vinyl-2-pyrrolidone)s: swelling behavior and water states. Macromol Biosci 2005;5:229–36.

[211] Read ML, Morgan PB, Kelly JM, Maldonado-Codina C. Dynamic contact angle analysis of silicone hydrogel contact lenses. J Biomater Appl 2011;26:85–99.

[212] Magin CM, Finlay JA, Clay G, Callow ME, Callow JA, Brennan AB. Antifouling performance of cross-linked hydrogels: refinement of an attachment model. Biomacromolecules 2011;12:915–22.

[213] Toworfe GK, Composto RJ, Shapiro IM, Ducheyne P. Nucleation and growth of calcium phosphate on amine-, carboxyl- and hydroxyl-silane self-assembled monolayers. Biomaterials 2006;27:631–42.

[214] Goda T, Konno T, Takai M, Moro T, Ishihara K. Biomimetic phosphorylcholine polymer grafting from polydimethylsiloxane surface using photo-induced polymerization. Biomaterials 2006;27:5151–60.

[215] Lin QK, Ding X, Qiu FY, Song XX, Fu GS, Ji J. In situ endothelialization of intravascular stents coated with an anti-CD34 antibody functionalized heparin-collagen multilayer. Biomaterials 2010;31:4017–25.

[216] Charbonneau C, Liberelle B, Hebert MJ, De Crescenzo G, Lerouge S. Stimulation of cell growth and resistance to apoptosis in vascular smooth muscle cells on a chondroitin sulfate/epidermal growth factor coating. Biomaterials 2011;32:1591–600.

[217] Pei J, Hall H, Spencer ND. The role of plasma proteins in cell adhesion to PEG surface-density-gradient-modified titanium oxide. Biomaterials 2011;32:8968–78.

[218] Lee HS, Eckmann DM, Lee D, Hickok NJ, Composto RJ. Symmetric pH-dependent swelling and antibacterial properties of chitosan brushes. Langmuir 2011;27:12458–65.

[219] Santonicola MG, de Groot GW, Memesa M, Meszynska A, Vancso GJ. Reversible pH-controlled switching of poly(methacrylic acid) grafts for functional biointerfaces. Langmuir 2010;26:17513–9.

[220] Blacklock J, You YZ, Zhou QH, Mao GZ, Oupicky D. Gene delivery in vitro and in vivo from bioreducible multilayered polyelectrolyte films of plasmid DNA. Biomaterials 2009;30:939–50.

[221] Cho WK, Kong B, Park HJ, Kim J, Chegal W, Choi JS, et al. Long-term stability of cell micropatterns on poly((3-(methacryloylamino)propyl)-dimethyl(3-sulfopropyl)ammonium hydroxide)-patterned silicon oxide surfaces. Biomaterials 2010;31:9565–74.

[222] Sapuri-Butti AR, Butti RC, Parikh AN. Characterization of supported membranes on topographically patterned polymeric elastomers and their applications to microcontact printing. Langmuir 2007;23:12645–54.

[223] Szmodis AW, Blanchette CD, Levchenko AA, Navrotsky A, Longo ML, Orme CA, et al. Direct visualization of phase transition dynamics in binary supported phospholipid bilayers using imaging ellipsometry. Soft Matter 2008;4:1161–4.

[224] Howland MC, Szmodis AW, Sanii B, Parikh AN. Characterization of physical properties of supported phospholipid membranes using imaging ellipsometry at optical wavelengths. Biophys J 2007;92:1306–17.

[225] Noel S, Liberelle B, Robitaille L, De Crescenzo G. Quantification of primary amine groups available for subsequent biofunctionalization of polymer surfaces. Bioconjug Chem 2011;22:1690–9.

[226] Ward J, Kelly J, Wang WX, Zeugolis DI, Pandit A. Amine functionalization of collagen matrices with multifunctional polyethylene glycol systems. Biomacromolecules 2010;11:3093–101.

[227] Coutinho DF, Pashkuleva IH, Alves CM, Marques AP, Neves NM, Reis RL. The effect of chitosan on the in vitro biological performance of chitosan-poly(butylene succinate) blends. Biomacromolecules 2008;9:1139–45.